Gold(I)-assisted catalysis – a comprehensive view on the [3,3]-sigmatropic rearrangement of allyl acetate

Marek Freindorf, Dieter Cremer & Elfi Kraka

Gold(I)-assisted catalysis – a comprehensive view on the [3,3]-sigmatropic rearrangement of allyl acetate

Marek Freindorf, Dieter Cremer† and Elfi Kraka

Computational and Theoretical Chemistry Group (CATCO), Department of Chemistry, Southern Methodist University, Dallas, TX, USA

ABSTRACT

The unified reaction valley approach (URVA) combined with the local mode, ring puckering and electron density analysis is applied to elucidate the mechanistic differences of the non-catalysed and the Au[I]-N-heterocyclic carbene (NHC)-catalysed [3,3]-sigmatropic rearrangement of allyl acetate. Using a dual-level approach (DFT and DLPNO-CCSD(T)), the influence of solvation, counter-ions, bulky and electron withdrawing/donating substituents as well as the exchange of the Au[I]-NHC with a Au[I]-phosphine catalyst is investigated. The catalyst breaks up the rearrangement into two steps by switching between Au[I]–π and Au[I]–σ complexation, thus avoiding the energy-consuming CO cleavage in the first step. Based on local stretching force constants k^a(C=C), we derive for the first time a quantitative measure of the π-acidity of the Au[I] catalyst; in all catalysed reactions, the bond order n(C=C) drops from 2 to 1.65. The ring puckering analysis clarifies that all reactions start and end via a six-membered ring with a boat form. All Au[I]–σ-complex intermediates show a considerable admixture of the chair form. The non-catalysed [3,3]-sigmatropic rearrangement goes through a maximum of charge separation between the allyl and acetate units at the transition state, while all catalysed reactions proceed via a minimum of charge separation reached in the region of the Au[I]–σ-complex.
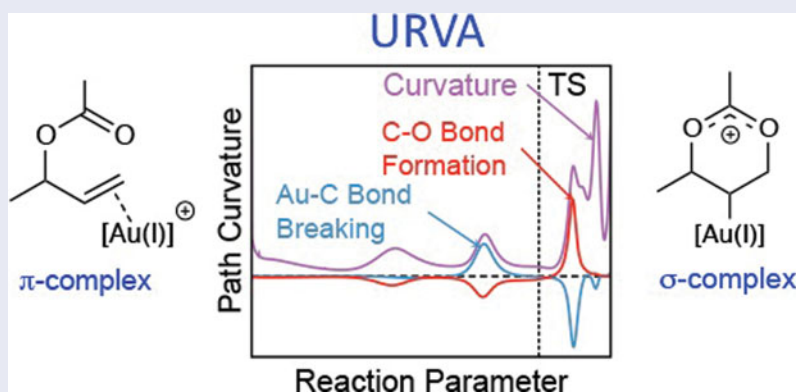
1. Introduction

Gold catalysis has attracted a lot of attention in the past two decades because it offers a large variety of organic transformations under mild reaction conditions and with high yields [1–12]. There exists an impressive diversity of reactions including the gold-catalysed assembly of complex molecules via C–H activation [13,14], cross-coupling reactions [14,15], or allylation reactions to densely functionalised compounds [16]. Gold has

physical and chemical properties which differ from other transition metals even from those of group 11 (Cu, Ag) caused by relativistic effects reaching a maximum at gold and platinum [17–19]. Because of these effects, the s- and p-orbitals shrink, lowering their orbital energy, while the d- and f-orbitals expand due to the increased shielding of the nuclear charge by the contracted s- and p-orbitals. This leads to an increased Au–ligand bond strength influencing its catalytic activity, which is often orthogonal to that of other transition metal catalysts [1,7]. The s-orbital

contraction and d-orbital expansion make cationic Au[I] species soft Lewis acids with high carbophilic character and a high affinity to coordinate with π-systems [17,18]. Therefore, cationic gold has proven in homogenous catalysis as an extraordinarily mild, yet effective, soft π-acid, capable of intra- or intermolecularly activating CC, CN or CO multiple bonds toward a nucleophilic attack [2,20–23].

Phosphines are one of the most common ligands applied in homogenous catalysis. They have been used with almost all metals including gold, and their chemistry is well known [10,24,25]. However, they are more and more replaced by N-heterocyclic carbenes (NHC) [26,27]. NHCs became predominant in catalysis after the isolation of a free NHC by Arduengo and co-workers [28,29] and subsequent pioneering work of Herrmann and co-workers [30]. NHC complexes of various transition metals are nowadays frequently used catalysts, in particular for the gold-catalysed activation of π-bonds [2,11,31–34]. The use of Au[I]-NHC catalysts offers a variety of advantages; NHCs are easier to make and store than their phosphine counterparts; they are less likely to dissociate from the metal during the reaction; they are stronger σ-donors than the most electron-rich phosphines and they show a much broader range of versatility and regio-selectivity as ligands [35].

Gold-catalysed sigmatropic rearrangements have been successfully employed in gold catalysis over the past decade [36]. However, not all mechanistic details of these processes are yet fully understood [21]. The Claisen rearrangement, introduced by Ludwig Claisen in 1902 [37], describes the [3,3]-sigmatropic rearrangement of allyl vinyl ethers leading to the preparation of γ, δ-unsaturated carbonyl compounds under the influence of heat. The synthetic potential of the Claisen rearrangement and related reactions has stimulated the interest of several generations of chemists to improve the yield of the rearrangement products, to shorten the reaction time and to perform the rearrangement under milder conditions to prevent undesired competitive side reactions and the decomposition of the starting materials and/or products. Claisen reported in his original paper [37] the apparent catalytic effect of ammonium chloride on the Claisen rearrangement, which was confirmed in 1963 [38]. Since then, numerous other substances including transition metal complexes have been tested as well as different environmental conditions, e.g. solvent effects, regarding their efficiency to catalyse the Claisen rearrangement and related sigmatropic shift reactions, to accelerate the reaction rates, and to increase the product specificity [36,39].

Recently, the gold-catalysed Claisen rearrangement of propargylic esters, which undergo intramolecular 1,2- or 1,3-ester migration, have attracted increasing attention

[2,7,16,40,41]. The same holds for their allylic counterparts, which provide an attractive access to oxo derivatives [42–44]. Nolan and co-workers [42] performed a DFT study of the Au[I]-NHC-catalysed [3,3]-sigmatropic rearrangement of allyl acetate focusing on the reaction energetics and the characterisation of the stationary points of the rearrangement reactions. They confirmed that the non-catalysed rearrangement proceeds in one step while the catalysed reaction proceeds in two steps via a Au[I]-acetonium intermediate (see Figure 1) [42]. They also tested the possibility that the catalyst coordinates to one of the oxygen centres. However, this led to unfavourable reaction barriers. This in line with the findings of Sieber and Tantillo [45] and the general understanding that Au[I] catalysts are predominantly carbophilic, while Au [III] species are considered as hard Lewis acids with a higher oxophilic character and a higher affinity to coordinate with more electronegative heteroatoms [6,18,46]. It is interesting to note that the general findings that NHC ligands and solvation effects have a strong impact on the rearrangement of allenyl vinyl ethers [10,40,47,48] were not confirmed for allyl acetate [42]. To clarify this obvious discrepancy, one has to understand more about the mechanistic features of these rearrangements. This implies that one goes beyond the investigation of just the stationary points. Therefore, in this work, we have performed an extensive study of the non-catalysed and catalysed [3,3]-sigmatropic rearrangement of allyl acetate exploring each reaction from the entrance to the exit channel.

The objectives of this study are the following: (i) to elucidate the mechanistic differences for the non-catalysed (reaction **R1**) and the catalysed (reactions **R2** -**R10**) [3,3]-sigmatropic rearrangements of allyl acetate in detail, in particular to review the current understanding that the catalytic effect of gold lies in its high ability to stabilise developing charges in the transition state (TS) region of the rearrangement paths [42–44]; (ii) to investigate the influence of the reaction medium on the rearrangement; solvation: reaction **R3**, inclusion of counter-ions: reaction **R4**, the influence of bulky NHC substituents: reaction **R5**, as well as the replacement of the Au[I]-NHC catalyst with a stronger Lewis acid such as Au[I]-phosphine: reaction **R6**, and the fine-tuning of the NHC ligand with electron-donating and electron-withdrawing groups: reactions **R7**–**R10**; (iii) to derive guidelines for a systematic improvement of the investigated Au[I] catalysts.

2. Computational methods

The major tool applied in this work is the *unified reaction valley approach* (URVA), which provides the study
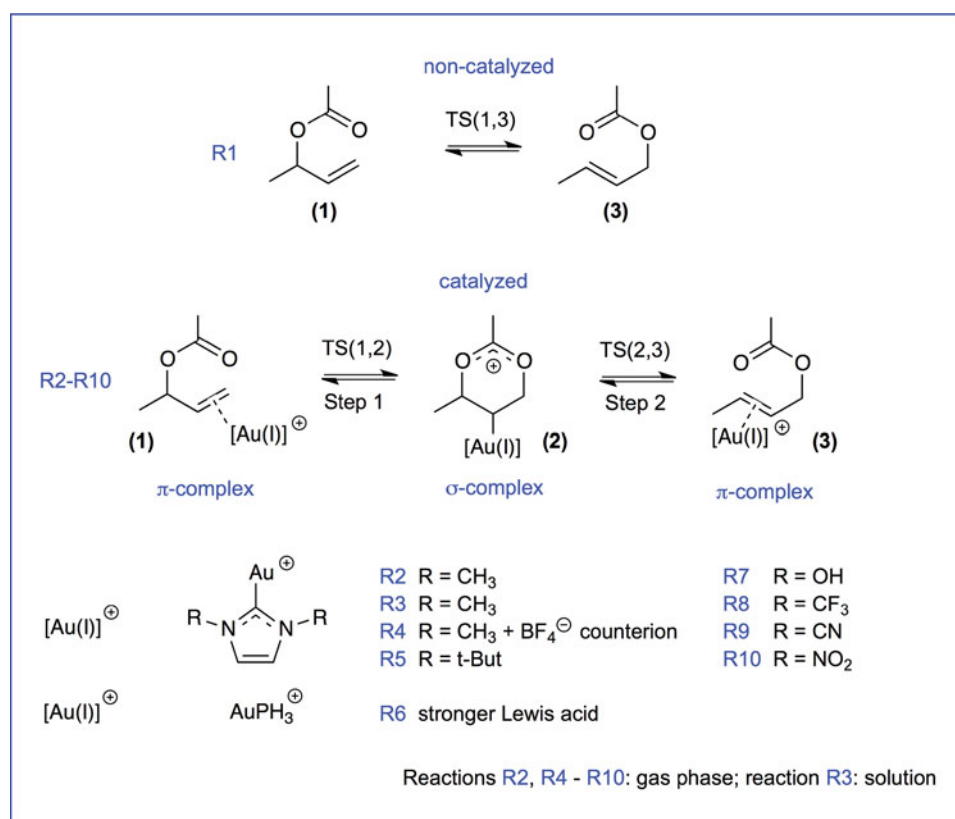
Figure 1. Reactions **R1**–**R10** investigated in this work.

of chemical reactions at a detail far beyond what conventional quantum chemical analyses of the reaction mechanism can offer [6,49–56]. URVA combines a quantum chemical description of the reaction complex (RC, the union of the reacting molecules) along the reaction path it traces during the reaction on the potential energy surface with elements of vibrational spectroscopy [49–52]. During the course of a chemical reaction, the RC changes its electronic structure and this is directly registered by the vibrational modes, which are sensitive to even the smallest electronic structure change [49]. The change in the vibrations leads to a change in the coupling with the translational motion of the RC along the reaction path. Following the procedure described by Handy, Miller, and Adams in their seminal *Reaction Path Hamiltonian* paper [57], we determine and monitor the different vibrational–translational couplings with the help of so-called curvature coupling coefficients $B_{\mu,s}$ which define the curving of the reaction path [49,50,57]. Therefore, the curvature of the reaction path directly reflects the change in the electronic structure of the RC. Each point along the reaction path is characterised in an URVA study by its distance from the TS given by the arc length s ($s = 0$ at the TS, with negative values in the entrance channel, $s < 0$; and positive values in the exit channel,

$s > 0$), the path direction given by the normalised path tangent vector $\eta(s)$ and the scalar path curvature $\kappa(s)$ which corresponds to the length of the curvature vector $\kappa(s)$ [49]. When we monitor $\kappa(s)$ along the reaction path, we obtain a curvature profile with curvature maxima Kn and minima Mn. Thus, we can divide the reaction into physically meaningful reaction phases with one phase stretching from Mn to $M(n + 1)$. The curvature minima Mn are indicative of a lower activity of RC (reduced vibrational–translational coupling) typically happening between two different chemical events. They can be associated with *hidden intermediates* or *hidden TSs* [52,53,56], which can be converted into real intermediates or TSs under specific reaction conditions, e.g. by adding a catalyst as investigated in this work. The curvature maxima Kn indicate electronic structure changes including bond-breaking/forming events, but also changes in charge transfer and charge polarisation, rehybridisation, changes in the optimal orientation of the reactants for the reactive collision, etc. These changes are further analysed by URVA via a decomposition of the curvature into local internal coordinate modes that have been defined recently [49]. These so-called curvature components characterise the electronic structure changes in terms of their magnitude and position along

the reaction path. Therefore, all chemical events can be located and described in detail as a function of the reaction path parameter s. The analysis of the curvature in terms of bond length, bond angle, and dihedral angle components can be complemented by a decomposition of the curvature into Cremer–Pople puckering coordinates [58–61]. In this way, conformational processes occurring during a chemical reaction, such as the conformational change of the six-membered ring of the allyl acetate during the [3,3]-sigmatropic rearrangement, can be quantitatively monitored.

Another important tool used in this work is the *local mode analysis*. Besides playing a key role for the URVA analysis, normal vibrational modes are a powerful starting point for the description of bond strength when converted into their local counterparts. Normal vibrational modes are generally delocalised because of mode–mode coupling. Therefore, they cannot directly be used to measure the intrinsic strength of a bond. There are two different coupling mechanisms between vibrational modes as a consequence of the fact that there is a kinetic and a potential contribution to the energy of a vibrational mode. Solving the Wilson equation of vibrational spectroscopy [62] involves a diagonalisation of the force constant matrix (potential energy part) and thus eliminates the so-called electronic coupling. However, the normal vibrational modes obtained in this way are still kinematically coupled (kinetic energy part) [63]. Elimination of the latter requires a reformulation of the Wilson equation by starting from the Euler–Lagrange equations in mass-decoupled form [63]. This leads to the Zou–Cremer local form of the Wilson equation, which can be solved to obtain electronically and kinematically decoupled local vibrational modes [64,65]. As shown by Zou, Cremer and co-workers, there is a 1:1 relationship between normal and local vibrational modes [64], and for each of the local modes, a force constant k^a, a frequency ω^a, a reduced mass, and an intensity [65] can be determined. Although not applied in this work, it is noteworthy that local mode frequencies can be obtained once normal-mode frequencies have been measured [66–68]. Zou and Cremer recently demonstrated that there is a direct relationship between the local stretching force constant k^a of a bond and its intrinsic strength [69]. Therefore, the local stretching force constant k^a is an ideal bond strength measure. It is used in this work to quantify the bond strength changes of the CO bonds directly involved in the rearrangement and to quantitatively access the strength of the Au[I]–ligand interaction in the π and σ complexes of reactions **R2**–**R10**. To simplify comparison, a relative bond strength order (BSO) n can be derived from the k^a values [70–73]. Utilising an extended Badger rule [68] according to which BSO n is related to the local

stretching force constant k^a, the following power relationship is obtained:

$$BSO\ n = A(k^a)^B.$$

The coefficients A and B are fully determined by two reference values and the requirement that for a zero-force constant n becomes zero. We used the following reference values in this work; CC bonds: $n = 1$ for the CC single bond in CH_3–CH_3 and $n = 2$ for the CC double bond in CH_2=CH_2; CO bonds: $n = 1$ for the CO single bond CH_3–OH and $n = 2$ for the CO double bond in CH_2=O; Au[I]–carbon bonds: $n = 1$ for the single bond in Au–CH_3 and $n = 2$ for the double bond in Pt=CH_2. This led to the following coefficients A and B; CC: $A = 0.35658$, and $B = 0.66679$; CO: $A = 0.32506$, and $B = 0.80158$; Au[I]C: $A = 0.57478$, and $B = 0.73466$ (see Figure S1, online supplemental data).

A dual-level strategy was pursued in this work. The reaction valley was evaluated at the DFT level while the energetics were calculated at the coupled cluster level of theory using the DFT geometries. This approach has proven as the best compromise for studying the mechanism of larger reaction systems while at the same time providing reliable energetics [6,54,74,75]. The following protocol was applied: URVA requires a representative path, which in this work was chosen to be the valley floor line. This is given by the IRC (intrinsic reaction coordinate) path of Fukui [76]. However, any other representative path, e.g. a downhill path from an energy plateau in the case of a barrierless reaction, can also be used [56,77] and insofar URVA is not limited to reactions with a TS. The IRC calculations were performed with the B3LYP density functional [78] using the Stuttgard–Dresden effective core potential (SDD) [79] with a corresponding basis set for the Au atom [80] and Pople's 6-31+G(d,p) basis set for all other atoms [81]. The calculations were performed using an ultrafine grid and a tight convergence criterion with a step size of $s = 0.03$ amu$^{1/2}$ Bohr applying the improved reaction path following procedure of Hratchian and Kraka, which allows to follow a chemical reaction far out into entrance and exit channel [82]. The reaction valley then was spanned by $3N$–L–1 normal coordinates (N, number of atoms; L, number of translations and rotations; 1 additional translation along the reaction path), which lead the harmonic vibrational modes of the RC orthogonal to the path; i.e. the reaction valley was described in the harmonic approximation. The corresponding energetics were calculated at the DLPNO-CCSD(T) level of theory [83,84] for the DFT geometries, using for Au the same basis set as for the DFT calculations, and the cc-pVQZ Dunning basis set for all other atoms [85–87]. The DLPNO-CCSD(T)

Table 1. Energetics (kcal/mol) for the [3,3]-sigmatropic rearrangements **R1** to **R10**[1].

React.	B3LYP 6-31+G(d,p) ΔE_{cp}[2]	B3LYP 6-31+G(d,p) Step 1		DLPNO-CCSD(T)/cc-pVQZ// B3LYP/6-31+G(d,p) Step 1						B3LYP 6-31+G(d,p) Step 2		DLPNO-CCSD(T)/cc-pVQZ// B3LYP/6-31+G(d,p) Step 2					
		$\Delta E^{\#}$	ΔE_R	$\Delta E^{\#}$	ΔE_R	$\Delta H^{\#}$	ΔH_R	$\Delta G^{\#}$	ΔG_R	$\Delta E^{\#}$	ΔE_R	$\Delta E^{\#}$	ΔE_R	$\Delta H^{\#}$	ΔH_R	$\Delta G^{\#}$	ΔG_R
R1	–	37.4	−0.6	45.9	0.7	44.1	0.9	45.9	1.2								
R2	−41.9	13.2	8.3	18.2	12.5	17.6	13.2	18.7	14.2	2.3	−9.2	3.8	−12.9	2.8	−13.3	2.9	−14.5
R3	−24.6	18.0	14.0	22.6	17.1	21.1	17.7	24.0	19.9	2.0	−14.7	4.0	−17.2	3.0	−17.6	2.8	−20.6
R4	−39.8	13.4	7.8	18.9	12.4	18.1	13.0	19.6	15.7	3.4	−8.0	5.4	−12.2	4.3	−12.8	3.0	−15.9
R5	−36.9	14.5	7.9	20.6	11.6	20.0	12.2	21.6	14.2	1.9	−6.4	4.1	−10.0	2.9	−10.5	2.4	−14.5
R6	−44.9	8.8	0.7	12.7	3.8	12.1	4.8	13.5	6.7	4.2	−2.3	6.3	−4.7	5.1	−5.9	4.9	−5.6
R7	−44.8	12.0	6.2	16.5	9.6	15.9	10.4	17.3	12.1	2.7	−7.6	5.2	−11.0	4.1	−11.5	3.9	−13.3
R8	−47.3	10.8	4.0	15.9	8.4	15.3	9.2	16.4	11.0	3.4	−5.3	5.4	−8.3	4.2	−8.8	3.4	−11.1
R9	−49.3	9.4	1.2	13.6	4.0	13.0	4.9	14.4	7.1	4.2	−2.7	7.5	−4.8	6.2	−5.4	5.6	−7.7
R10	−48.5	10.6	3.8	15.5	8.3	15.0	9.2	16.2	10.6	3.4	−5.2	5.7	−8.7	4.5	−9.2	4.2	−10.9

[1]Activation energies, $\Delta E^{\#}$, enthalpies $\Delta H^{\#}$ and free energies $\Delta G^{\#}$; reaction energies ΔE_R, enthalpies ΔH_R and free energies ΔG_R. For the coupled cluster enthalpies and free energies, the DFT thermochemistry was used.
[2]Complexation energy calculated as the difference between the energy of the RC and the sum of the energies of the gold catalyst and the allyl acetate calculated for the geometry of first point on the IRC in the entrance channel. Basis set superposition error corrected via the counterpoise method of Boys and Bernardi [94].

enthalpies and free energies were based on the B3LYP/6-31+G(d,p) thermochemistry. For reaction **R3**, the polarisable continuum solvent model (PCM) of Tomasi and co-workers [88] was used for the DFT calculations applying a dielectric constant of 10.36 for dichloroethane. The energetics were calculated at the DLPNO-CCSD(T)/cc-pVQZ:COSMO// B3LYP/6-31+G(d,p):PCM level of theory with the SDD effective core potential for Au, and using the conductor-like screening model (COSMO) of Klamt and co-workers [89]. The URVA and local mode analysis were carried out with the program COLOGNE16 [90]. For the coupled cluster calculations, the program ORCA [83] was used, whereas the DFT calculations were carried out with Gaussian09 [91]. Natural bond orbital (NBO) charges were calculated with the program NBO 6 [92], and the electron density analysis was performed with the program AIMALL [93].

3. Results and discussion

In the following, the results from this study will be presented. First, the energetics of the reactions **R1**–**R10** will be discussed, followed by a local mode analysis describing in particular the strength of the Au–carbon interactions. Then, the URVA analysis of reactions **R1**–**R6** will be presented and complemented by an analysis of the energy contribution to each of the reaction phases, a ring-puckering analysis and the elucidation of charge transfer and charge polarisation along the rearrangement path.

3.1. Reaction energetics

In Table 1, the energetics of reactions **R1**–**R10** are summarised for both the DFT and the DLPNO-CCSD(T)

level of theory. For the first endothermic step of the catalysed [3,3]-sigmatropic rearrangement, the activation energies $\Delta E^{\#}$ are 4–6 kcal/mol too low at the DFT level of theory. For the second exothermic step with much lower energy barriers, the DFT activation energies are 1.5–3.5 kcal/mol too low. This confirms the general finding that DFT overestimates the effects of electron correlation, in particular for TSs leading often to barriers which are significantly too low [95,96]. However, as reflected by the data in Table 1, the general trends for reactions **R1**–**R10** are correctly reproduced by DFT confirming the validity of our dual-level approach.

The non-catalysed reaction **R1** proceeds in one step (see Figure 1) with a DLPNO-CCSD(T) activation energy $\Delta E^{\#}$ of 45.9 kcal/mol and a reaction energy ΔE_R of 0.7 kcal/mol compared with a $\Delta E^{\#}$ value of 37.4 kcal/mol and ΔE_R value of −0.6 kcal/mol at the DFT level. A barrier of this height prevents the non-catalysed reaction from being useful in synthesis. The catalysed reactions **R2**–**R10** proceed in two steps as illustrated in Figure 1, in agreement with previous studies [42,45]. The gold moiety coordinates to the π-electrons of the alkene forming a π complex with complexation energies of up to −49 kcal/mol in the gas phase and −25 kcal/mol in solution (see Table 1) reflecting the high carbophilicity of the gold[I] catalyst [97]. Reaction **R2** with the simplest Au[I]-NHC catalyst shows a significant lowering of the reaction barrier of the non-catalysed reaction **R1**. With a $\Delta E^{\#}$ value of 18.2 kcal/mol (DLPNO-CCSD(T); DFT 13.2 kcal/mol), the first reaction step leads to a σ-bonded gold complex which is 12.5 kcal/mol (DLPNO-CCSD(T); DFT 8.2 kcal/mol) less stable than the π-complex. The second step transforming the σ-bonded gold intermediate into the final π-complex is highly exothermic by 12.9 kcal/mol
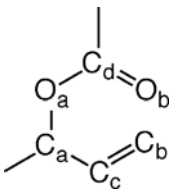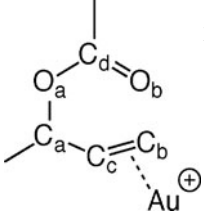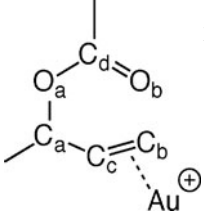
(DLPNO-CCSD(T);DFT 9.2 kcal/mol; Table 1) and proceeds with a small barrier of only 3.8 kcal/mol (DLPNO-CCSD(T); DFT 2.3 kcal/mol). The catalysed reaction **R3** in the weakly polar solvent dichloroethane has with of 22.6 kcal/mol (DLPNO-CCSD(T); DFT 18.0 kcal/mol), the highest barrier among reactions **R2**–**R10**, indicating that solvation in a weakly polar solvent does not support a further lowering of the reaction barrier. Experimentally, the gold catalyst is introduced into the reaction in the form of a chloride salt that then reacts with silver tetrafluoroborate [7,34,98]. Given the positive charge of the catalyst and the low polarity of the solvent, the reacting system is likely associated to a tetrafluoroborate anion after the precipitation of silver chloride. Counteranions have been found to critically affect organometallic processes by forming hydrogen bonds with the organic substrate [99]. However, reaction **R4** has almost the same barrier as reaction **R2** (18.9 kcal/mol DLPNO-CCSD(T); 13.4 kcal/mol DFT) suggesting that the net effect of all stabilising interactions with the counter-ion does not change significantly during the chemical reaction. Introducing bulky t-But groups on the NHC (reaction **R5**) leads to a small increase of the barrier by 2.4 kcal/mol. Since the NHC plane is orthogonal to the plane of the 1,3-acetoxonium moiety, bulkier t-But groups experience hardly any steric hindrance explaining the similar energetics of reactions **R2** and **R5**. Au[I]-phosphine and Au[I]-NHC-complexes show a remarkable reactivity difference in the case of the gold-catalysed Claisen rearrangement of allenyl vinyl ethers [21,48]. Along these lines, we find the lowest reaction barrier of 12.7 kcal/mol (DLPNO-CCSD(T);DFT 8.8 kcal/mol; Table 1) for the first step for reaction **R6** (exchange of the Au[I]-NHC with Au[I]-PH$_3$. On the other hand, reaction **R6** has the highest barrier for the second step (6.3 kcal/mol (DLPNO-CCSD(T);DFT 4.2 kcal/mol; Table 1). We further tested whether replacing the methyl substituent of the NHC in reaction **R2** with either electron-donating substituents (OH: reaction **R7**) or electron-withdrawing substituents (CF$_3$: reaction **R8**; CN: reaction **R9**; NO$_2$: reaction **R10**) could lead to any significant change of the reaction energetics. Compared with reaction **R2**, we found for the first step, a decrease of the activation energy $\Delta E^{\#}$ of 1.7, 2.3, 4.6, and 2.7 kcal/mol for reactions **R7**, **R8**, **R9** and **R10**, respectively (DLPNO-CCSD(T) level of theory) and an increase of the activation energy $\Delta E^{\#}$ in the range of 1–3 kcal/mol for the second step. These results suggest the Au[I]-phosphine catalyst as the best option within the gold[I] catalysts investigated in this work. The energetics allow to test the overall performance of a catalyst; however, they do not provide a detailed rational. This will be targeted in the following by the local mode analysis.

3.2. Relative bond strength orders

Understanding the nature of the metal–ligand interactions plays an important role for the fine-tuning of the reactivity of the metal centre and the development and design of new and more efficient catalysts. In order to elucidate the Au[I]–carbon interaction in the [3,3]-sigmatropic rearrangement, we applied the local mode analysis to all reactants, intermediates and products of reactions **R1**–**R10**, complemented with the topological analysis of the electron density distribution $\rho(\mathbf{r})$ [100]. In particular, the nature of the Au[I]–carbon interaction in the π- and σ-gold complexes was determined with the energy density H$_c$ calculated at the bond critical point $\mathbf{r}_c$ and the application of the Cremer–Kraka criteria for covalent bonding: (i) a zero-flux surface and bond critical point $\mathbf{r}_c$ have to exist between the atoms in question (necessary condition for covalent bonding). (ii) The local energy density H$_c$ must be negative and thereby stabilising (sufficient condition for covalent bonding). A positive H$_c$ indicates a dominance of electrostatic interactions [101,102]. Hence, the Cremer–Kraka criteria can reveal whether the Au[I]–carbon interaction is covalent, electrostatic, or a mixture of both (H$_c$ values close to zero).

In Table 2, the local mode analysis and the electron density analysis data for reactions **R1**, **R2**, and **R6** are summarised. The corresponding data for reactions **R3**–**R5** and **R7**–**R10** are collected in Tables S1–S7 (online supplemental data). The data in Table 2 show the expected bonding pattern for the non-catalysed reaction **R1**. The two double bonds CcCb and CdOb in the reactant molecule **1** have a BSO close to 2 and the two single bonds CcCa and CdOa in resonance with the double bonds have BSOs slightly larger than 1. The central CaOa bond, which has to be broken during the rearrangement, is the longest and weakest bond (n = 0.8) which should favour the rearrangement. The starting point for the rearrangement is nucleophilic attack of the CdOb unit towards the CcCb π bond. Therefore, the central role of the Au[I] catalyst is to accept electron density from the CcCb π system, thus weakening the CcCb π bond, and in this way activating it for the nucleophilic attack. This is for the first time quantified by the local mode analysis. As revealed by the data of Table 2, gold-complexation of **1** has a strong effect on the CcCb π bond. The CcCb π bond increases in length (0.041 Å in reaction **R2**; 0.042 Å in reaction **R6**), and, most importantly, the BSO decreases from 1.98 to 1.65 for both reactions, **R2** and **R6** (see Table 2). The weakening is also reflected by the adjacent CcCa single bond, which becomes longer (0.018 Å in reactions **R2** and **R6**) and a slightly weaker (n = 0.98 in reaction **R2**; 0.96 Å in reaction **R6**). Interesting to note is that the same

Table 2. Bond length R, local mode force constants k^a, local modes frequencies ω^a, C–C, C–O, and Au–C bond orders BSO n, electron density ρ_c at the bond critical point $\mathbf{r}_c$, and energy density H_c at the bond critical point $\mathbf{r}_c$ of the reactant **1**, the intermediate **2**, and the product **3** for the [3,3]-sigmatropic rearrangements **R1**, **R2** and **R6** calculated at the B3LYP/6-31+G(d,p)/SDD(Au) level of theory.

Numbering/reaction	Molecule	Bond	R (Å)	k^a (mDyn/Å)	ω^a (cm^{-1})	n	ρ_c (e/Bohr^3)	H_c (Hartree/Bohr^3)
R1	**1**	C_c–C_b	1.335	9.537	1642.5	1.98	0.346	−0.387
		C_c–C_a	1.505	4.315	1104.8	1.05	0.263	−0.222
		C_d–O_b	1.214	12.191	1737.2	1.89	0.413	−0.714
		C_d–O_a	1.356	5.274	1142.6	1.08	0.298	−0.465
		C_a–O_a	1.466	3.352	910.9	0.80	0.226	−0.289
	3	C_c–C_b	1.499	4.455	1122.5	1.08	0.264	−0.224
		C_c–C_a	1.338	9.326	1624.2	1.95	0.344	−0.384
		C_d–O_b	1.355	5.314	1147.0	1.09	0.413	−0.714
		C_d–O_a	1.214	12.201	1737.9	1.89	0.299	−0.467
		C_b–O_b	1.460	3.506	931.6	0.82	0.229	−0.298
R2	**1**	C_c–C_b	1.376	7.566	1463.0	1.65	0.325	−0.341
		C_c–C_a	1.523	3.942	1056.0	0.98	0.256	−0.212
		C_d–O_b	1.213	12.175	1736.1	1.89	0.411	−0.701
		C_d–O_a	1.370	4.716	1080.5	1.00	0.288	−0.442
		C_a–O_a	1.451	3.699	956.9	0.85	0.237	−0.315
		Au–C_b	2.279	0.830	352.9	0.50	0.076	−0.020
		Au–C_c	2.343	0.619	304.8	0.40	–	–
		Au–π	2.207	1.061	290.1	0.60	–	–
	2	C_c–C_b	1.497	4.033	1068.1	0.99	0.263	−0.231
		C_c–C_a	1.499	3.861	1045.1	0.96	0.263	−0.231
		C_d–O_b	1.284	7.803	1389.8	1.40	0.348	−0.573
		C_d–O_a	1.279	7.953	1403.1	1.42	0.352	−0.583
		C_a–O_a	1.575	1.148	533.1	0.39	0.167	−0.148
		C_b–O_b	1.533	1.725	653.4	0.51	0.185	−0.194
		Au–C_c	2.133	1.802	519.9	0.89	0.112	−0.045
	3	C_c–C_b	1.518	4.084	1074.8	1.00	0.255	−0.212
		C_c–C_a	1.381	7.342	1441.1	1.61	0.323	−0.336
		C_d–O_b	1.369	4.806	1090.7	1.02	0.289	−0.446
		C_d–O_a	1.214	12.198	1737.7	1.89	0.410	−0.700
		C_b–O_b	1.442	3.943	988.0	0.89	0.241	−0.329
		Au–C_c	2.291	0.802	346.9	0.49	0.076	−0.020
		Au–C_a	2.353	0.596	299.0	0.39	–	–
		Au–π	2.217	1.048	288.3	0.59	–	–
R6	**1**	C_c–C_b	1.377	7.562	1462.5	1.65	0.325	−0.341
		C_c–C_a	1.523	3.880	1047.6	0.96	0.255	−0.213
		C_d–O_b	1.212	12.224	1739.5	1.89	0.412	−0.702
		C_d–O_a	1.375	4.546	1060.9	0.98	0.285	−0.435
		C_a–O_a	1.448	3.758	964.5	0.86	0.240	−0.320
		Au–C_b	2.288	0.749	335.2	0.46	0.074	−0.018
		Au–C_c	2.379	0.492	271.7	0.34	–	–
		Au–π	2.230	0.993	280.7	0.57	–	–
	2	C_c–C_b	1.501	4.080	1074.3	1.00	0.261	−0.227
		C_c–C_a	1.505	3.933	1054.8	0.97	0.261	−0.225
		C_d–O_b	1.285	7.912	1399.5	1.42	0.347	−0.571
		C_d–O_a	1.280	8.048	1411.5	1.43	0.351	−0.580
		C_a–O_a	1.561	1.403	589.3	0.45	0.173	−0.163
		O_b–C_b	1.523	1.985	700.9	0.56	0.189	−0.208
		Au–C_c	2.125	1.849	526.8	0.90	0.114	−0.046
	3	C_c–C_b	1.521	3.994	1062.9	0.99	0.254	−0.210
		C_c–C_a	1.385	7.244	1431.5	1.59	0.322	−0.334
		C_d–O_b	1.371	4.693	1077.8	1.00	0.263	−0.234
		C_d–O_a	1.213	12.193	1737.3	1.89	0.411	−0.701
		C_b–O_b	1.439	4.009	996.1	0.90	0.244	−0.334
		Au–C_c	2.293	0.741	333.4	0.46	0.075	−0.019
		Au–C_a	2.389	0.481	268.7	0.34	–	–
		Au–π	2.237	1.004	282.2	0.58	–	–
References	C_2H_6	C–C	1.533	4.063	1072.1	1	0.241	−0.191
	C_2H_4	C=C	1.334	9.647	1651.9	2	0.345	−0.388
	C_3OH	C–O	1.425	4.695	1078.0	1	0.254	−0.359
	CH_2O	C=O	1.209	13.277	1812.9	2	0.409	−0.692
	$AuCH_3$	Au–C	2.044	2.125	564.7	1	0.129	−0.061
	$PtCH_2$	Au=C	1.799	5.459	905.3	2	0.221	−0.154

pattern is found for all other catalysed reactions investigated in this work (see Tables S1–S7, online supplemental data).

The local mode analysis was combined with the electron density analysis to provide specific information about the nature of the Au[I]–ligand interaction. The gold atom gets closer to the terminal Cb than to the central Cc atom (2.279 Å versus 2.343 Å reaction **R2**; 2.288 Å versus 2.379 Å reaction **R6**). We find a weak covalent Au–Cb bond, as reflected by the negative H_c value of −0.020 Hartree/Bohr^3 and a bond order of 0.5 while no covalent bond is formed between Au and Cc, as revealed by the data in Table 2. So despite the fact that in the Au[I]–σ complex the gold atom is bonded to the central carbon atom Cc, first a stronger Au[I]–Cb interaction takes place. In the intermediate Au[I]–σ complex **2**, the covalent Au[I]–Cc bond is fully established with a bond order of 0.89 and a negative H_c value of −0.045 Hartree/Bohr^3, reaction **R2** ($n = 0.9$, $H_c = −0.046$ Hartree/Bohr^3, reaction **R6**). The two CO bonds of the acetate unit equalise with bond distances of 1.284 and 1.279 Å and bond orders of 1.4, reaction **R2**; 1.285 and 1.280 Å and bond orders of 1.42, reaction **R6**. The two central CO bonds CaOa and CbOb of intermediate **2** become long, 1.575 and 1.533 Å and weak, $n = 0.4$ and 0.5, reaction **R2** (1.561 and 1.523 Å and $n = 0.5$ and 0.6, reaction **R6**) confirming the characterisation of complex **2** as a six-membered ring stabilised 1,3-acetoxonium ion (see Figure 1). A similar bonding pattern as for the reactant Au[I]–π complex **1** is found for the product Au[I]–π complex **3**. Although the terminal Ca atom in **3** has a methyl group attached, the Au[I] still prefers a shorter and stronger interaction with the Ca atom first leading to a covalent bond. The characteristic weakening of the CcCb double bond and the approach of the gold atoms to the terminal C atom of the double bond was found for all reactions investigated in this work (**R3**–**R5** and **R7**–**R10**, Tables S1–S7, online supplemental data). To better understand why the Au[I] first attaches with the terminal Cb atom before forming a σ bond with the central Cc atom and why the catalytic activity of the different Au[I] complexes used in reactions **R2**–**R10** seems to be the same, URVA analyses monitoring the whole reaction from the entrance to the exit channel were performed for reactions **R1**–**R6**.

3.3. Curvature profiles and reaction mechanism

In the following, the curvature profiles of reactions **R1**–**R6** will be discussed with a focus on the elucidating the mechanistic differences between non-catalysed and catalysed reactions. In Figure 2, the scalar reaction path curvature and its decomposition into those internal coordinate components, which dominate the

[3,3]-sigmatropic rearrangement along the reaction path, is shown for reactions **R1**–**R6**. Videos following the evolution of the RC along the reaction path are provided for reactions **R1**–**R6** in the online supplemental data.

3.3.1. Non-catalysed reaction

The curvature diagram of the non-catalysed reaction **R1** is shown in Figure 2(a). Reaction **R1** proceeds via 10 reaction phases being characterised by nine curvature minima M1–M9 with six distinct curvature peaks K1–K6. Because of the improved reaction path following algorithm [82], the stereo-chemical details of the rearrangement in the entrance and exit channels become visible leading to the following mechanism: phases 1 and 2 are characterised by the rotation of methyl groups and the acetate unit, while phase 3 is characterised by a pseudo-rotation of the six-membered ring bringing the Cb and Ob atoms closer together (see video R1, online supplemental data). The CbOb bond to be formed (Figure 2(a)) already contributes to the pre-chemical phases 2–4; first resisting in phase 2 (negative contribution), then supporting in phase 3 (positive contribution) and resisting again in phase 4. Phase 5 is dominated by the cleavage of the CaOa bond causing the curvature peak K3 (Figure 2(a)) with a small supporting contribution of the CdOb bond and a small resisting contribution of the CdOa bond which has to transform into a double bond during the rearrangement. In phase 6, characterised by a small and broad curvature peak K4 containing the TS, the RC adapts a boat form with CaOa and CbOb distances close to 2.1 Å. Both the CaOa and the CbOb bonds are resisting a further change in this phase (see video R1, online supplemental data) indicating the possibility to break up the reaction in this area into two steps, e.g. with a catalyst. In Phase 7, leading to the curvature peak K5, the formation of the new CbOb bond is the dominating event with a small supporting contribution of the CaOa bond and a small resisting contribution of the CdOb bond, which has to transform into a double bond in the case of the reverse reaction. Phases 8–10 are characterised by six-membered ring pseudo-rotations and a rotation of acetate methyl-group. In summary, the most important curvature peaks are K3: entrance channel, breakage of the CaOa bond, K4 around the TS: bringing the RC into a boat form with equal CaOa and CbOb bond lengths, and K5: exit channel, formation of the new CbOb bond.

3.3.2. Au(I)-catalysed reaction

In Figure 2(b,c), the curvature diagrams of step 1 and step 2 of the Au(I)-NHC-catalysed reaction **R2** are shown. The first step starts from the π-bonded complex with the gold attached to the CcCb double bond of the allyl
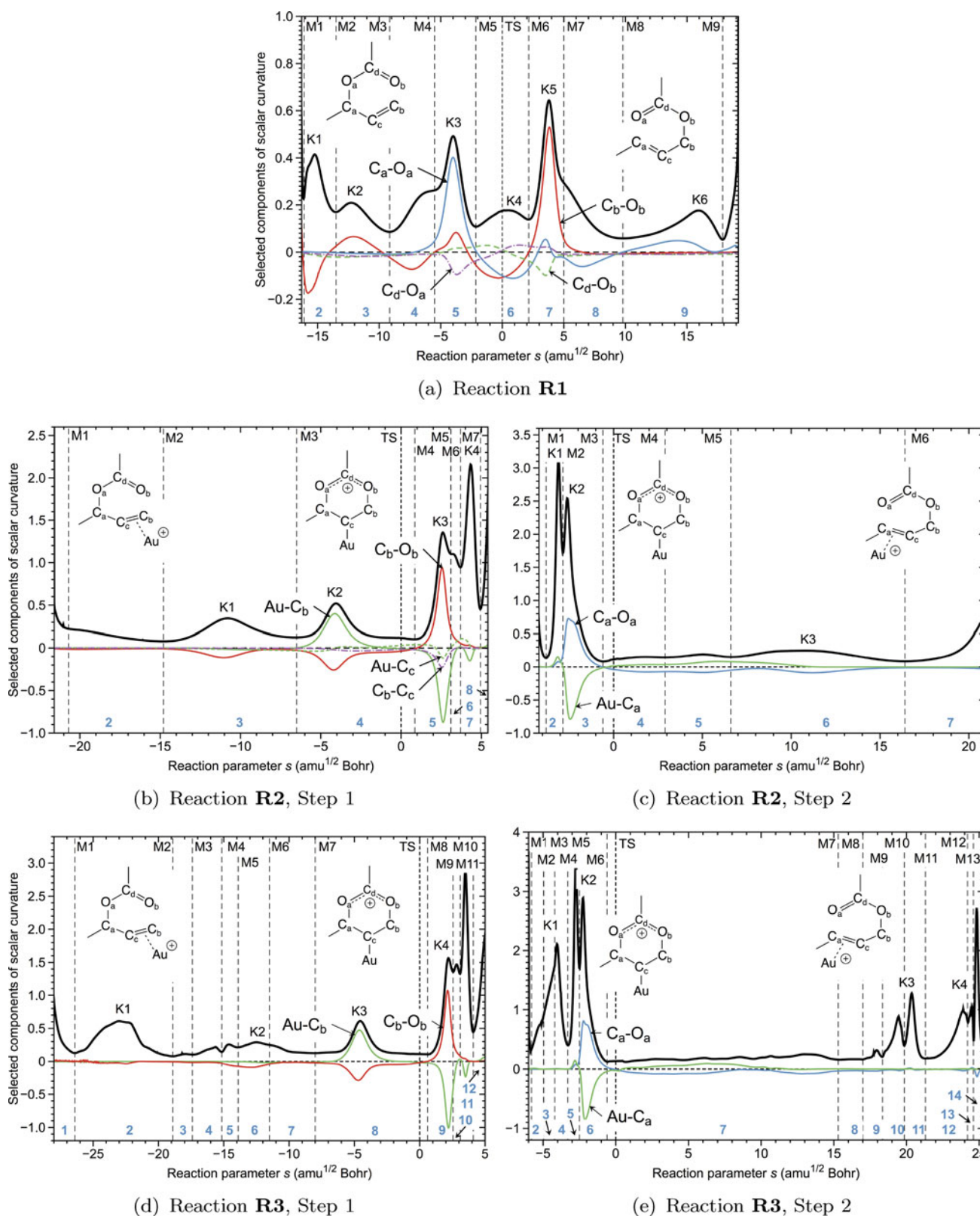
Figure 2. Scalar curvature as a function of the reaction path parameter s (solid black line) for the [3,3]-sigmatropic rearrangements **R1**–**R6**. The decomposition of the scalar curvature into components. The borders of the reaction phases are indicated by vertical dashed lines at curvature minima M1, M2, M3, etc. Curvature maxima are given as K1, K2, K3, etc. The TS at $s = 0$ amu$^{1/2}$ Bohr is also indicated by a vertical dashed line. B3LYP/6-31+G(d,p)/SDD(Au) level of theory.
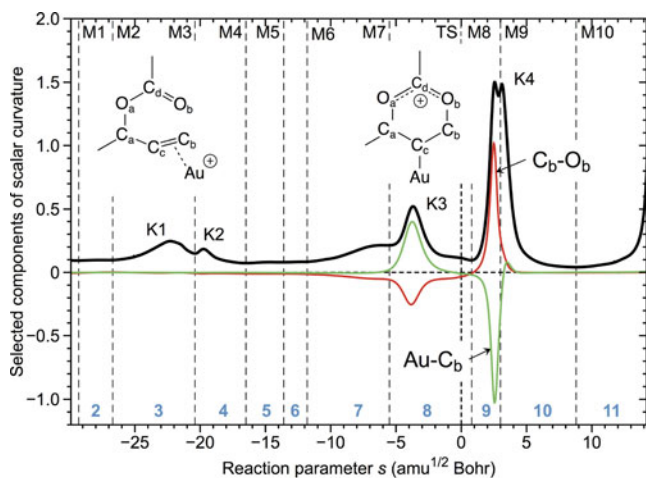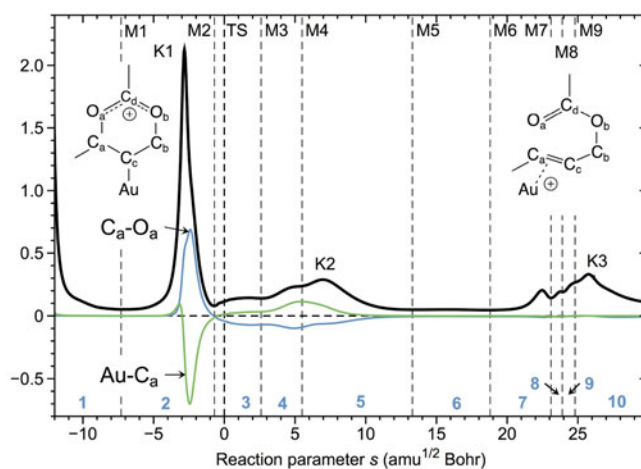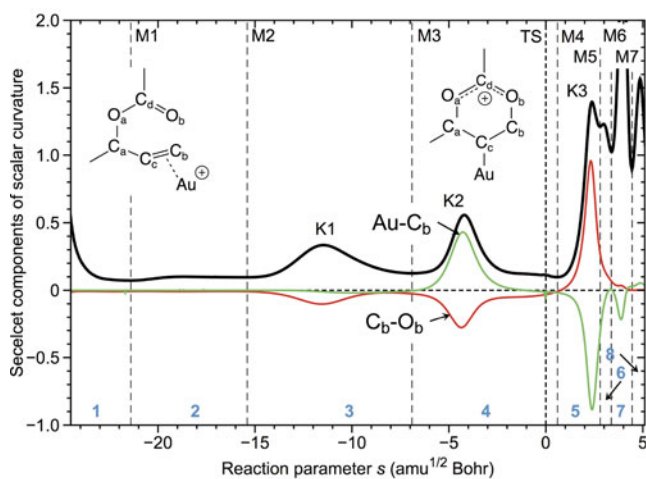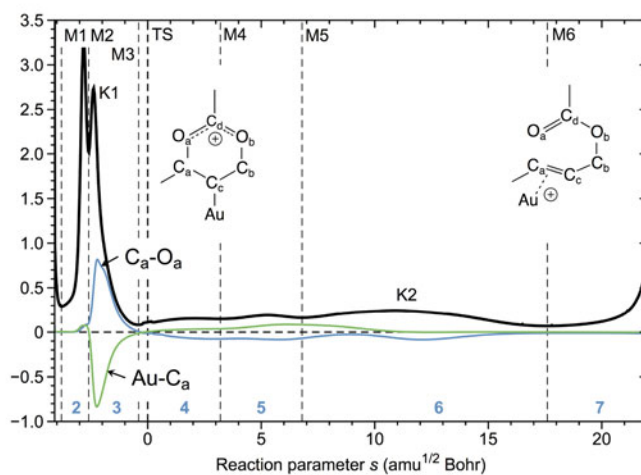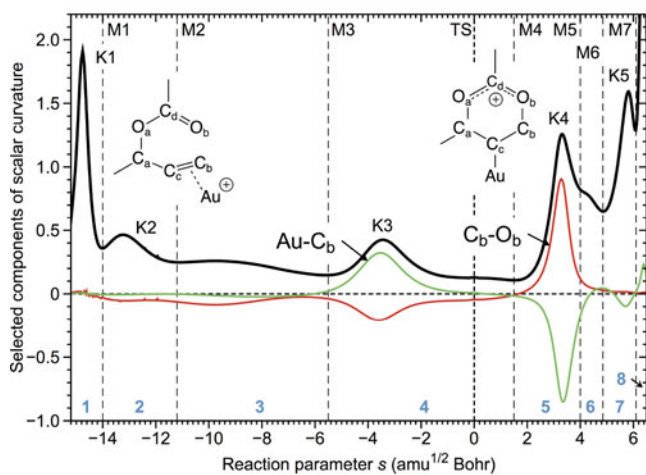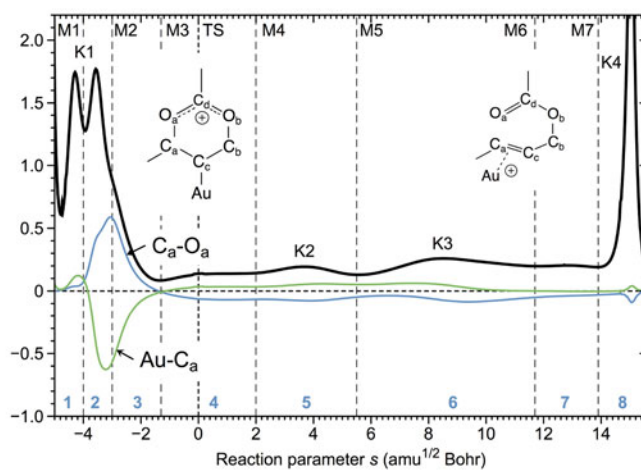
(f) Reaction **R4**, **Step1**

(g) Reaction **R4**, **Step2**

(h) Reaction **R5**, Step 1

(i) Reaction **R5**, Step 2

(j) Reaction **R6**, Step 1

(k) Reaction **R6**, Step 2

Figure 2. (Continued.)

acetate and ends with the formation of an intermediate σ-bonded complex Au(I) complex with both the CaOa to be broken still intact and the new CbOb bond formed, thus resembling the TS of the non-catalysed reaction. We identify eight phases and four distinct curvature peaks (see Figure 2(b)). The entrance channel of step 1 is about 10 s units longer compared with that of the non-catalysed reaction. Before the TS, there are only two smaller curvature enhancements; K1 is characterised by the resistance of the CbOb bond to be formed and the rotation of the methyl groups similar to K1 for the non-catalysed reaction, K2 is dominated by the loosening of the Au(I)–Cb interaction (Figure 2 (b)) and a continued resistance of the CbOb bond to be formed. At K2, both Au–carbon distances become almost equal, while at the beginning of step 1, the Au–Cb distance is shorter than the Au–Cc distance, although at the end of this step, the Au–Cc σ-bond is established. It is interesting to note that we still find at K2 a bond critical point and a bond path between Au–Cb and not, as one may expect because of the bond equalisation at that curvature peak, a bond path between both Au–carbon atoms (see Figure S3, online supplemental material). After K2, the Au–Cb distance increases while the Au–Cc distance stays almost the same. The Au atom pushes the Cb atom closer to the Ob atom and in this way mediates the formation of the new CbOb bond. The CaOa bond to be broken does not contribute to the curvature in contrast to the non-catalysed reaction **R1**. After the TS in phase 5, the new CbOb is formed (peak K3) while phases 6–8 are characterised by methyl group adjustments and smaller pseudo-rations of the six-membered ring (see video R2, online supplemental data). Since the formation of the Au(I)–σ-complex is endothermic by 12.5 kcal/mol (DLPNO-CCSD(T)), the regeneration of a stable Au(I)-π-complex proceeds in step 2 (see Figure 2(c)) via establishing the new AuCa interaction, which simultaneously weakens and breaks the CaOa bond (peak K2), a process which is initiated in phase 1 by a pseudo-rotation of the six-membered ring and which stretches over the whole exit channel characterised by small, energy saving pseudo-rotations of the six-membered ring as well as adjustments of the NHC part.

The curvature profiles for step 1 and step 2 of reaction **R3** are shown in Figure 2(d,e). Both the pre-chemical phases of step 1 and the post-chemical phases of step 2 are much longer than those of reaction **R2**, which is typical of a reaction in solution. The broad curvature peak K1 at −22 s units is characterised by NHC methyl groups rotations and pseudo-rotation of the six-membered ring which have to adjust for the rearrangement out of the equilibrium conformation in the solvent. The remaining curvature profile resembles strongly that of reaction **R2** confirming that the solvent does not change the actual

rearrangement mechanism. The same hold for step 2. The mechanism of the regeneration of the stable Au(I)–π-complex and the cleavage of the CbOb bond at K2 remain unchanged; however, the exit channel stretches further out with several pronounced curvature peaks reflecting the rotation of the NHC moiety and the pseudo-rotation of the six-membered ring into the equilibrium conformation of the product in solution (see video R3, online supplement data).

The counter-ion effect on the [3,3]-sigmatropic rearrangement investigated in reaction **R4** leads to the curvature profiles shown in Figure 2(f,g). The curvature profile of step 1 has an extended pre-chemical phase (phases 1–4), resembling the solution curvature profile; however, the curvature peaks are less pronounced. The BF_4^- counterion forms in this region five hydrogen bonds with the reaction complex. Three of them are formed with allyl hydrogens (average $F{\cdots}H$ distance: 2.37 Å, average local force constant: 0.043 mDyn/Å), and two hydrogen bonds are formed with the NHC methyl hydrogen atoms (average $F{\cdots}H$ distance: 2.39 Å, average local force constant: 0.029 mDyn/Å). In the exit channel, the BF_4^- counterion moves closer to the allyl acetate part forming two hydrogen bonds (average $F{\cdots}H$ distance: 2.16 Å, average local force constant: 0.083 mDyn/Å), and one hydrogen bond with the NHC methyl hydrogen atom ($F{\cdots}H$ distance: 2.34 Å, local force constant: 0.042 mDyn/Å). Additionally, there is a relatively strong electrostatic interaction between one fluorine atom of the BF_4^- counter and the positively charged carbon Cd located between the oxygen atoms of acetate part (the $F{\cdots}C$ distance: 2.76 Å, local force constant: 0.087 mDyn/Å (see Figure S2 and Table S8, online supplemental data). In step 2 of this reaction, the BF_4^- counter-ion moves back closer to the NHC part of the catalyst, forming six hydrogen bonds. Four of them are formed with the hydrogen atoms of allyl acetate (average $F{\cdots}H$ distance: 2.53 Å, average local force constant: 0.036 mDyn/Å), and two of them are formed with the NHC methyl hydrogen atoms (the average $F{\cdots}H$ distance: 2.39 Å, and the average local force constant: 0.030 mDyn/Å). The calculated bond orders of these hydrogen bonds are smaller than 0.1, which indicates that the interaction between the BF_4^- counterions and the reaction complex has a dominant electrostatic character. As obvious from video R4 (online supplemental data), the counter-ion always adjusts during the rearrangement reaction to find the optimum number of H-bond interactions with the Au(I)-complex. These hydrogen bonds embrace the NHC and 1,3-acetoxonium moieties restricting their conformational flexibility. However, this does not lead to a change of the overall rearrangement mechanism. The curvature profile of step 2 of reaction **R4** shows only one pronounced peak in the

entrance channel dominated by the breakage of the CaOa bond. The pre-chemical region is much shorter than that of reaction **R3**, while the post-chemical region shows some curvature enhancements far out in the exit channel predominantly caused by a rotation of NHC methyl group in contact with the BF_4^- counter-ion. In summary, the reaction phases describing the bond-breaking and bond-forming processes are dominated by the same components as in reaction **R3** illustrating that the neither solvent nor counter-ion effects lead to significantly different mechanistic features of the catalysed rearrangements.

The effect of bulky NHC substituents tested in reaction **R5** leads to curvature profiles (Figure 2(h,i)) which are almost identical with those obtained for the methyl substituted system. This confirm previous findings that because of the structural arrangement of the NHC perpendicular to the plane of the 1,3-acetoxonium moiety, bulky groups have no influence on the reaction mechanism [42].

In reaction **R6**, we tested whether the replacement of the Au[I]-NHC complex with a stronger Lewis acid can lead to a change in the rearrangement mechanism. The curvature profiles of steps 1 and 2 of reaction **R6** (Figure 2(j,k)) clearly suggest that this is not the case. The overall curvature profiles of both steps and their decomposition pattern resemble those of reaction **R2**. Noteworthy are the large curvature peaks K1 at −15 s units in the entrance channel of step 1 and K4 at 15 s units in the exit channel of step 2, which result, in both cases, from rotations of the PH_3 unit (see video R6, supplemental data).

In summary, the curvature profiles reveal that the catalytic action of the gold(I) catalyst of allyl acetate is due to (1) the formation of a stable sigma-bonded intermediate avoiding to start with an energy-consuming breakage of the CaOa bond; (2) the simplification of the ring pseudo-rotation (the boat form is relaxed in the TS region) and (3) the assistance of gold with the breaking and forming of the CO bonds.

Once the reaction phases are determined with URVA, the mechanistic details obtained from the curvature profiles can be complemented by the analysis of the energy contribution to the reaction barrier in each reaction phase, as shown in Figure 3(a,b), and Table 3 for the non-catalysed reaction **R1** and the first step of the catalysed reaction **R2**. Since all chemical events taking place before the TS cost energy, this analysis provides a quick access to identifying these events. Together with the mechanistic knowledge gained from the curvature analysis, this can serve as a useful starting point for optimising and tuning the reaction, e.g. via a catalyst. In both cases, the pre-chemical phases 1–3 contribute with less than 3.5 kcal/mol to the barrier, denoting that the rotation and adjustment of the methyl groups is independent of the

Table 3. Energy contribution (kcal/mol) of each reaction phase to the reaction barrier for the [3,3]-sigmatropic rearrangements of reaction **R1** and the first step of reaction **R2**. B3LYP/6-31+G(d,p)/SDD(Au) level of theory.

	Reaction **R1**			Reaction **R2** (Step 1)	
Phase	Energy[a]	Energy[b]	Phase	Energy[a]	Energy[b]
1	0.0	0.0	1	0.0	0.0
2	0.3	0.3	2	0.3	0.3
3	3.1	3.4	3	3.0	3.3
4	7.1	10.5	4	9.9	13.2 (TS)[c]
5	18.4	28.9			
6	8.5	37.4 (TS)[c]			

[a] Energy contribution of the reaction phase.
[b] Energy at the end of the reaction phase.
[c] Up to the TS contained in this phase.

catalyst. In reaction **R1**, this is followed by 7.1 kcal/mol in phase 4 needed to rotate the reaction complex into a form which is necessary to start the CaOa bond breaking. Phase 5, the actual CaOa bond-breaking phase, has with 18.4 kcal/mol the largest contribution to the energy barrier. In contrast, there is only one more phase before the TS in the case of reaction **R2**, phase 4 contributing with 9.9 kcal/mol to the barrier resulting from the breakage of the Au(I)Cb interaction.

3.4. Puckering analysis

A large number of theoretical investigations of [3,3]-sigmatropic rearrangements suggest a concerted rearrangement through a chair-like TS [103,104]. However, there are exceptions such as the Ireland–Claisen rearrangement which favours a boat TS over a chair-like TS in the case of steric hindrance [105]. Often a quantitative measurement of the ring puckering and its influence on the rearrangement mechanism is not provided. Therefore, in the following section, we will couple URVA with the Cremer–Pople puckering analysis [58–60] to elucidate the changes of the puckering of the intermediate six-membered ring during the catalysed and non-catalysed [3,3]-sigmatropic rearrangement of allyl acetate.

The Cremer–Pople puckering analysis [58–60] offers an important tool for the quantitative description of conformational changes during chemical reactions involving ring systems. For six-membered rings, the puckering analysis is based on the puckering amplitudes q_2 and q_3, the pseudo-rotation phase angle Φ_2, the hyperspherical angle Θ, and the total puckering amplitude Q. They are split into the pseudo-rotational coordinate pair (q_2, Φ_2) describing the pseudo-rotation of boat and twist-boat forms of the six-membered ring, and the single crown puckering amplitude q_3, which describes the chair (positive q_3) and inverted chair form (negative q_3). Based
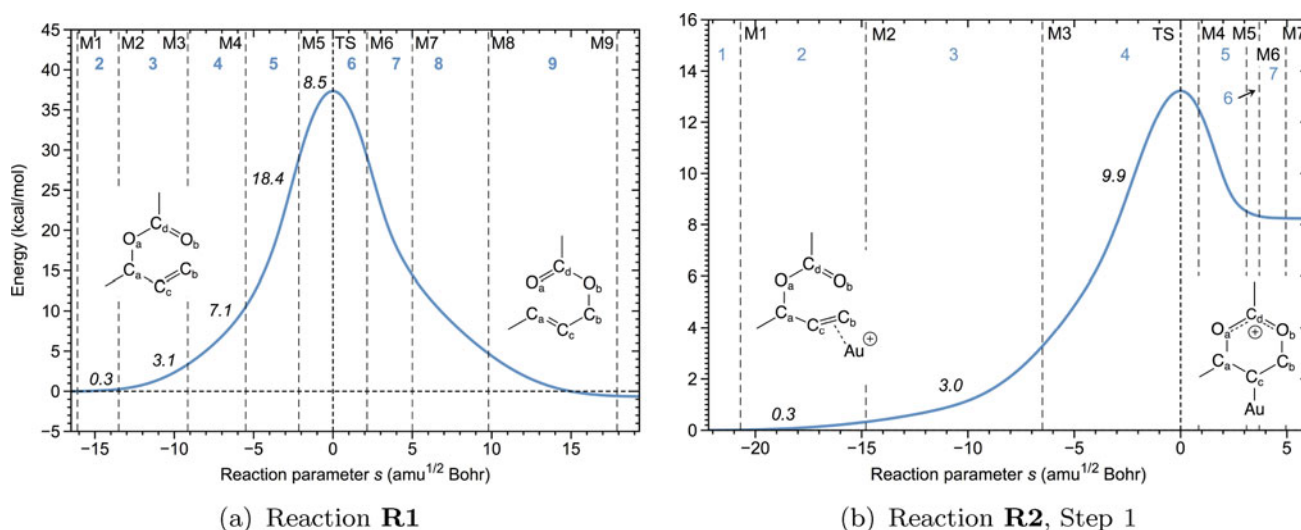
Figure 3. Energy profile with energy contributions (the italics numbers) to the reaction barrier in each reaction phase for the [3,3]-sigmatropic rearrangements **R1** and **R2** (Step 1). The borders of the reaction phases are indicated by vertical dashed lines at curvature points M1, M2, M3, etc., and the reaction phases are indicated by the bold numbers. The TS at $s = 0$ amu$^{1/2}$ Bohr is also indicated by a vertical dashed line. B3LYP/6-31+G(d,p)/SDD(Au) level of theory.

on values of these puckering coordinates, the contributions of chair, boat and twist-boat forms can be predicted according to the following formulas [58,60]:

$$\text{Chair}: 100\%\frac{q_3^2}{Q^2},$$

$$\text{Boat}: 100\%\frac{q_2^2}{Q^2}\cos^2(3\Phi_2),$$

$$\text{Twist boat}: 100\%[1 - \cos^2(3\Phi_2)]\frac{q_2^2}{Q^2}.$$

In Figure 4, the changes of the puckering coordinates along the reaction path for the [3,3]-sigmatropic rearrangements **R1** and **R2** are shown. In Table 4, the percentages of the chair, boat and twist-boat forms for the stationary points of reactions **R1**–**R6** are summarised. According to the puckering analysis, the RC of the non-catalysed reaction **R1** is changing from an initial structure with 85.7% boat and 11.8% twist-boat contributions via a TS with predominant boat form (89.9%) and 9.7% admixture of chair form to the final structure with 83.2% boat and 14% twist boat (see Figure 4(a)). The contribution of the chair form is less than 10%. The catalysed reactions show a different puckering pattern. The first step of the catalysed reaction **R2** starts with an almost pure boat form (99.0%) and leads to an intermediate with 67.6% boat form and 32.1% chair form (see Figure 4(b)). The second step of this reaction ends with a reaction complex being composed of 96.7% boat form again (see Figure 4(c)). While in the non-catalysed reaction **R1**, the boat form has to be maintained during the

Table 4. Contribution of the chair, boat and twist-boat forms (in percentage) to the six-membered ring of molecules **1**, **TS(1,3)**, and **3** of reaction **R1**; molecules **1**–**3** of reactions **R2**–**R6**.

Reaction	Molecule	Chair	Boat	Twist boat
R1	**1**	2.5	85.7	11.8
	TS(1,3)	9.7	89.9	0.4
	3	2.7	83.2	14.1
R2	**1**	1.0	99.0	0.0
	2	32.1	67.6	0.3
	3	1.8	96.7	1.5
R3	**1**	0.9	99.0	0.1
	2	32.6	67.2	0.2
	3	1.2	97.2	1.6
R4	**1**	6.2	75.2	18.6
	2	53.4	46.6	0.0
	3	12.1	38.0	49.9
R5	**1**	0.8	99.1	0.1
	2	32.0	67.6	0.4
	3	1.7	96.9	1.4
R6	**1**	1.7	97.6	0.7
	2	32.7	67.2	0.1
	3	2.5	93.8	3.7

rearrangement keeping the two CO bonds be broken and formed together, this is accomplished in the catalysed reactions by forming a stable Au[I]–σ complex. While reactions **R3**, **R5**, and **R6** show the same puckering pattern, reaction **R4** behaves somewhat different, which is a result of the BF_4^- counter-ion hydrogen bonding, restricting the conformational flexibility of the RC. In particular, the puckering of complexes **1** and **3** of reaction **R4** is different because of the different hydrogen bond pattern (see Table S8 and Figure S2, online supplementary data).

We can also decompose the reaction path curvature into puckering components to learn about the influence

(a) Reaction **R1**

(b) Reaction **R2**, Step 1

(c) Reaction **R2**, Step 2

(d) Reaction **R2**, Step 1
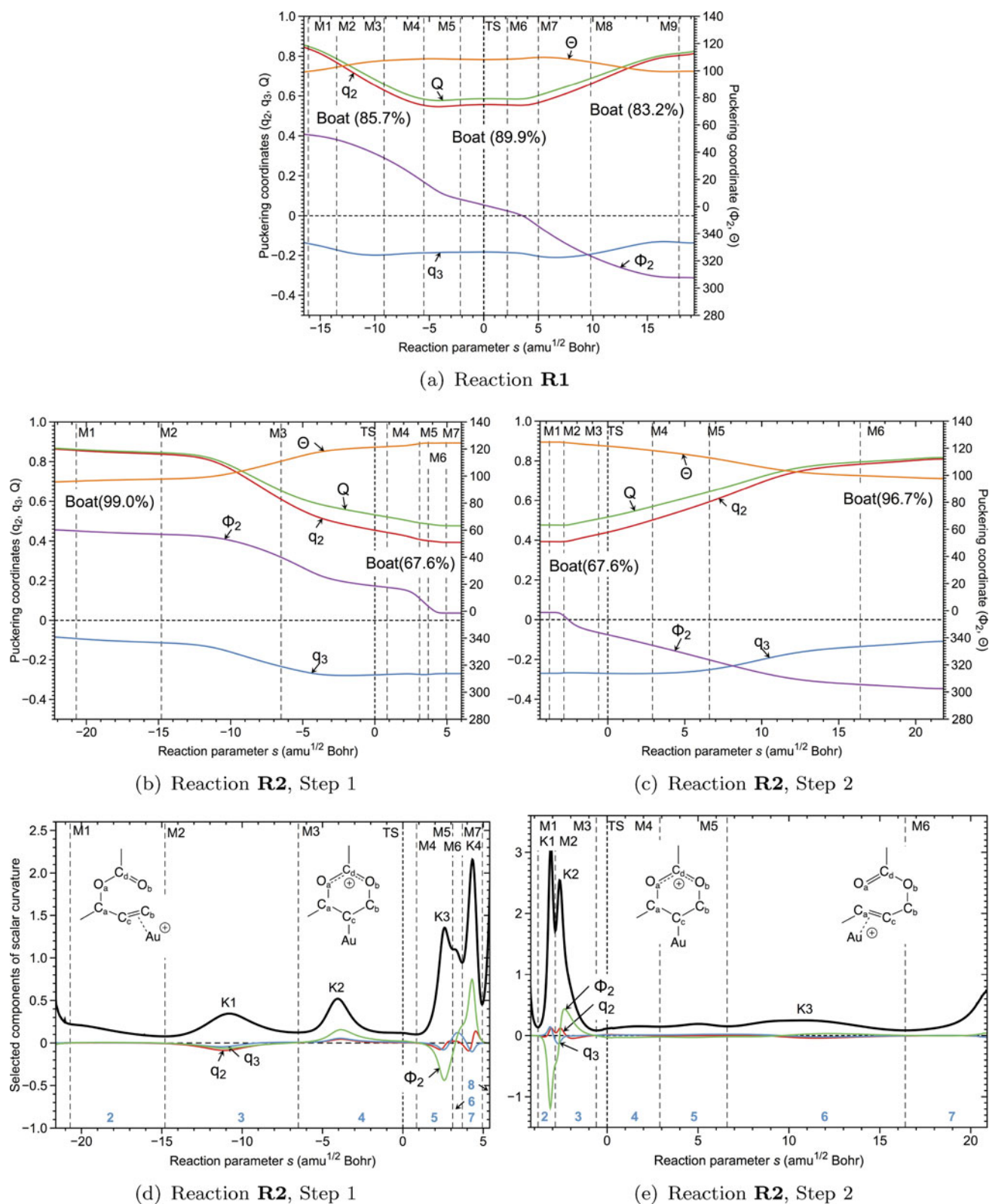
(e) Reaction **R2**, Step 2

Figure 4. (a–c) Changes of the puckering coordinates along the reaction path for the [3,3]-sigmatropic rearrangements of reaction **R1** and the two steps of reaction **R2**; (d,e) decomposition of the reaction path curvature into puckering coordinates for the two steps of reaction **R2**. The borders of the reaction phases are indicated by vertical dashed lines at curvature points M1, M2, M3, etc. The TS at $s = 0$ amu$^{1/2}$ Bohr is also indicated by a vertical dashed line. B3LYP/6-31+G(d,p)/SDD(Au) level of theory.

(a) Reaction **R1**

(b) Reaction **R2**, Step 1
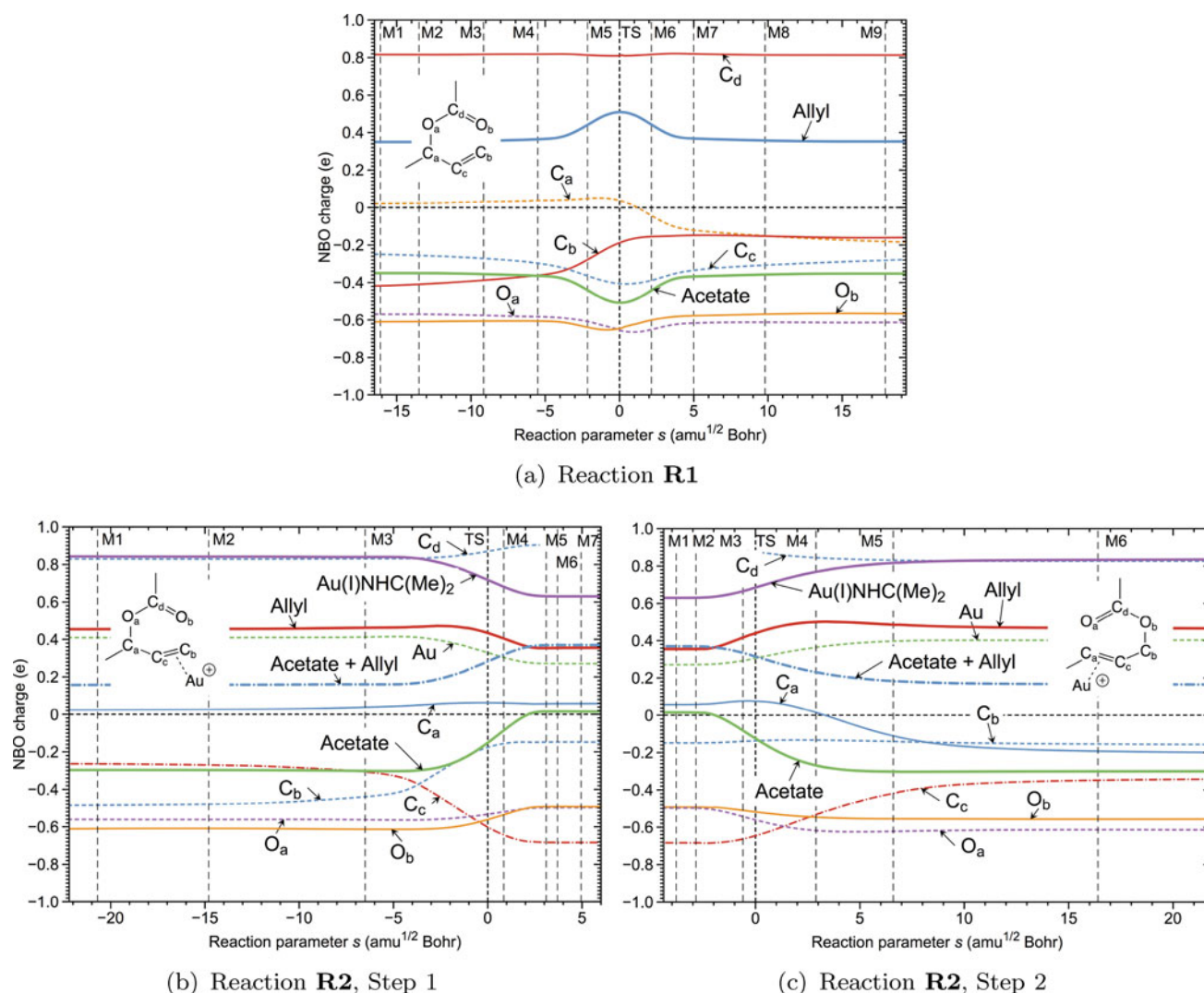

(c) Reaction **R2**, Step 2

Figure 5. NBO charges along the reaction path for the [3,3]-sigmatropic rearrangements **R1** and **R2**. The borders of the reaction phases are indicated by vertical dashed lines at curvature points M1, M2, M3, etc. The TS at $s = 0$ amu$^{1/2}$ Bohr is also indicated by a vertical dashed line. B3LYP/6-31+G(d,p)/SDD(Au) level of theory.

of ring puckering on the reaction mechanism, as shown for the steps of reaction **R2** in Figure 4(d,e). The curvature peaks K3 and K4, phases 5–7, have strong contributions of the pseudo-rotation phase angle Φ_2. In this region, Φ_2 shows a sudden drop from 20° to 0° (see Figure 4(b)). In step 2, curvature peaks K1 and K2 are characterised by strong Φ_2 contributions again in a region of sudden change of Φ_2. In summary, the catalysed reactions show a considerable admixture of the chair form in the intermediate **2** (30%–50%; see Table 4), which is the lowest energy conformation of the three six-membered ring forms [60].

3.5. Charge transfer and polarisation along the rearrangement path

We will complete the URVA study with the analysis of the charge transfer and charge polarisation along the reaction

path. In Figure 5, the changes of the NBO charges along the reaction path are shown for reactions **R1** and **R2**. In Figure 6, the NBO charges of the atoms involved in the rearrangement of reactants **1**, products **3**, the **TS(1,3)** for reaction **R1** and intermediates **2** for reactions **R2** and **R6** are summarised. The NBO charges of the C and O atoms involved in the rearrangement as well as the total charge of the allyl fragment and that of the acetate fragment for the non-catalysed reaction **R1** are shown as a function of s in Figure 5(a). At the beginning of the rearrangement, the acetate part is negatively charged by -0.350 e (charge of the central Cd atom: 0.816 e, Oa: -0.570 e and Ob: -0.610 e; see Figure 6). At the TS, the negative charge of the acetate part reaches a maximum of -0.509 e. Both oxygens are switching their role at the TS, Oa becomes more negative, Ob becomes more positive (see Figure 6(a)). The charges at the terminal
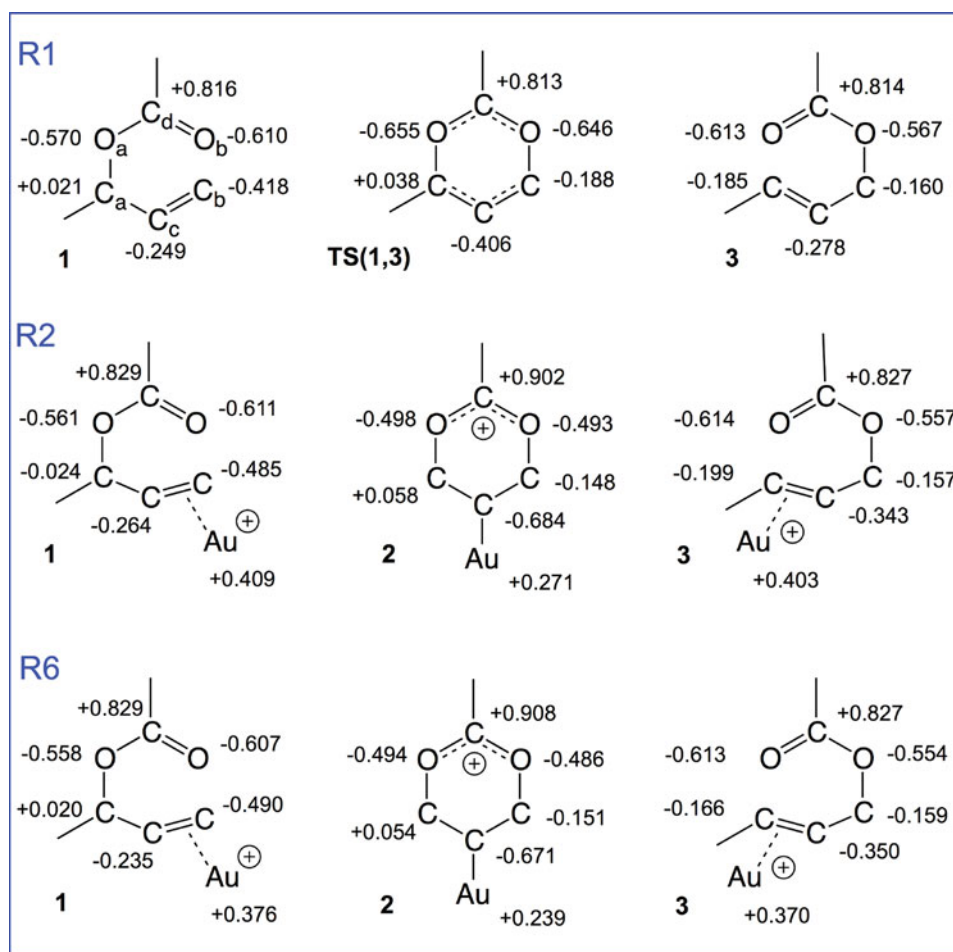
Figure 6. NBO charges of molecules **1**, **TS(1,3)**, **3**, reaction **R1**; NBO charges of molecules **1**, **2**, **3**, reactions **R2** and **R6**. B3LYP/6-31+G(d,p)/SDD(Au) level of theory.

carbon atoms of the allyl part start to equalise, Ca, being slightly positively charged (0.021 e) in **1** has a negative charge of −0.185 in **3** as a consequence of losing the bond with Oa and adapting more sp^2 character. The opposite is the case for carbon Cb (−0.418 e in **1** versus −0.160 e in **3**; see Figure 6). The positive charge of 0.816 e of the central C atom Cd of the acetate fragment does not change during the rearrangement while the central carbon Cc of the allyl fragment drops down from −0.249 e to −0.406 e at the TS. It is interesting to note that the charge difference between the allyl and the acetate fragments of 0.700 e remains constant in the first four phases, then starts to increase in phase 5, with the breaking of the CaOa bond, goes through a maximum of 1.018 e at the TS, and decreases to its final value of 0.704 e in phase 7, with the formation of the new CbOb bond. This confirms that the TS can be viewed as an anionic acetate fragment interacting with a positive carbocation as postulated by Nolan and co-workers [42]. Moreover, the URVA analysis shows that

the charge transfer between the two fragments occurs synchronously with the bond-breaking and bond-forming events.

Figure 5(b,c) shows the charge analysis of steps 1 and 2 of the catalysed reactions **R2** and **R6**. The allyl fragment is more positively charged (0.445 e compared with 0.350 e in reaction **R1**) while the acetate fragment is slightly less negatively charged (−0.300 e compared with −0.350 e in reaction **R1**). So in total, the allyl acetate picks up a considerable portion (0.145 e) of the positive charge of the Au[I]-NHC catalyst. In the middle of phase 4 ($s = -3.5$ s units), the charge pattern starts to change in concert with the loosening of Au–Cb interaction. Both, the Au[I]-NHC catalyst and the allyl fragment withdraw charge from the acetate fragment. This process is finished at the end of phase 5 ($s = 3.1$ s units), which is characterised by the formation of the new Cb–Ob bond and the establishment of the Au–Cc σ bond. In this connection, Cc becomes more negatively charged (−0.264 e for **1** compared with −0.684 e at the end of phase 5).
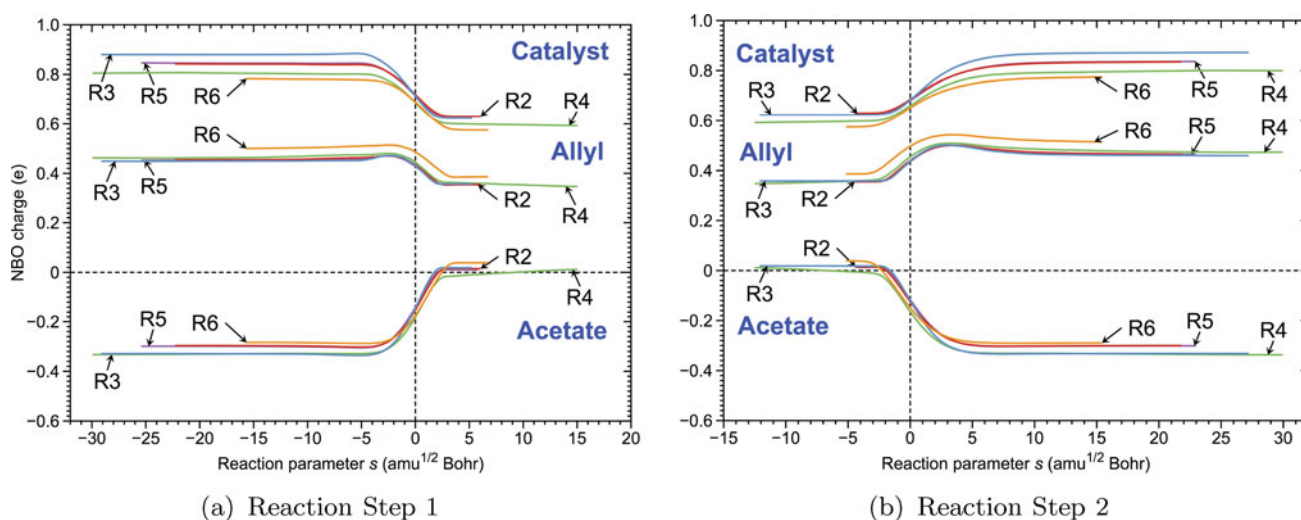
Figure 7. NBO charges along the reaction path for the [3,3]-sigmatropic rearrangements **R2**–**R6**. The TS at $s = 0$ amu$^{1/2}$ Bohr is indicated by a vertical dashed line.

Ob and Cb both become less negative (Ob -0.493, Cb -0.148 e, compared with -0.611 and -0.485 e for **1**) and less repulsive supporting the formation of the new CO bond. Step 1 of the reaction **R2** ends at the intermediate **2** corresponding to **TS(1,3)** in the non-catalysed reaction. In contrast to reaction **R1**, the intermediate **2** is characterised by the smallest charge separation between the acetate and allyl fragments (0.363 e in contrast to 1.018 e in **TS(1,3)**). Interesting to note is also that the charge transfer between these fragments is reversed. While in reaction **R1** at **TS(1,3)** the acetate fragment adapts a maximum of negative charge and the allyl fragment a maximum of positive charge, in **2** of reaction **R2**, both fragments adapt their minimum charge. The same holds for the gold atom. In the σ-complex **2**, the Au[I] charge is reduced from 0.409 e (**1**) to 0.271 e (see Figure 6). The central carbon atom Cd of the acetate receives a positive charge of 0.902 e in **2**. Therefore, it is justified to label **2** as acetonium ion. In phase 3 ($s = -3$ s units) of step 2 (see Figure 5 c) which is characterised by the breakage of the CaOa bond and the regeneration of the Au(I) π complex, the charge transfer starts to proceed back in the opposite direction. At the end of phase 5, the final charge distribution of **3** is reached. While in the case of the non-catalysed reaction the rearrangement goes through a maximum of charge separation between the allyl and acetate units at the TS, as suggested by Nolan and co-workers [42], the catalysed reaction proceeds via a minimum of charge separation reached in the region of the Au[I]σ-bonded intermediate. This shows the important influence of the gold catalyst on the electronic structure changes during the rearrangement, guiding the forming and breaking of the CO bonds in the most energy-saving way.

One important feature of URVA is that different chemical reactions can directly be compared. This is a result of using a reaction path in mass-weighted coordinates. Therefore, instead of discussing each reaction separately, we can overlay the changes of the NBO charges of the RC along the reaction path for different reactions. Figure 7 reveals that the changes in the charge distribution along the rearrangement path show the same trends for the catalytic reactions **R2**–**R6** despite the different environments or the exchange of the NHC ligand with a phosphine ligand.

During step 1, the gold catalyst accepts ca. 0.2 e charge from the allyl acetate in the small region of ± 3 s units around the TS, with most of the charge being transferred from the acetate part. This transfer is reversed in step 2 again happening in a small region of ± 2 s units around the TS and being coupled with CO bond formation and bond breaking and the transformation between the Au[I]-π and Au[I]-σ complex.

4. Conclusions and outlook

This work has demonstrated that URVA combined with the local mode, the ring puckering and the topological electron density analysis forms an excellent toolbox to unravel the mechanistic features of catalytic reactions. The application of this toolbox to the non-catalysed and the Au[I]-catalysed [3,3]-sigmatropic rearrangement of allyl acetate has led to the following conclusions.

(1) The URVA analysis reveals that the Au[I] catalyst breaks up the non-catalysed rearrangement into two steps by acting as a chameleon, e.g.

easily switching between Au[I]–π and Au[I]–σ complexation. Gold docks to the ethylene unit in the first step by forming a Au[I]–π-complex, guides the formation of the new CO bond while leaving the CO bond to be broken still intact, and transforms at the end of this step into an intermediate Au[I]–σ-complex resembling the TS of the non-catalysed reaction. In the second step, the Au[I]–σ-complex transforms back into a more stable Au[I]–π-complex supporting CO bond cleavage.

(2) All chemical events take place before the TS cost energy. The energy decomposition into reaction phases allows a quick access to identifying these events. In the case of the non-catalysed rearrangement, the cleavage of the CaOa bond in phase 5 has with 18.4 kcal/mol, the largest contribution followed by 8.5 kcal/mol in phase 6, necessary to keep the RC in the boat form. These events are avoided in the first step of the catalysed reaction.

(3) The Au[I]-phosphine catalyst (reaction **R6**) turns out as the best option within the gold[I] catalysts investigated in this work lowering the original barrier of 45.9 kcal/mol to 12.7 kcal/mol (step1, DLPNO-CCSD(T)).

(4) The local stretching force constants k^a and the related BSO n are introduced as quantitative measure of the π-acidity of the Au[I] catalyst. For all catalysed reactions investigated in this work, the $n(C=C)$ value drops down from 2 to 1.65 revealing that differences in the π-acidity do not have a significant influence on CC double bond weakening.

(5) The topological analysis of the electron density discloses the nature of the Au[I]–carbon interaction. The Au–carbon bond in the Au[I]–σ-complex is identified as covalent σ bond with a bond order n of 0.9. Noteworthy is that in the case of the Au[I]–π-complex, only a weak covalent Au–Cb bond ($n = 0.5$) is found in step 1, but no Au–Cc bond. Although in the Au[I]–σ-complex the gold atom binds to the central carbon atom Cc, first a stronger Au[I]–Cb interaction takes place.

(6) The ring-puckering analysis reveals that all rearrangements investigated in this work start and end with a six-membered ring with more than 90% boat form. While the boat form is kept in the non-catalysed reaction, all intermediate Au[I]–σ-complexes have a considerable admixture of the chair form, the lowest of the three six-membered ring forms. A decomposition of the reaction path curvature into puckering components reveals that the pseudo-rotation phase angle Φ_2 contributes significantly to the curvature in both entrance and exit channels.

(7) A direct comparison of the NBO analysis of all catalysed reactions along the reaction path discloses another common feature of the Au[I] catalysts. While in the case of the non-catalysed reaction the rearrangement goes through a maximum of charge separation between the allyl and acetate units at the TS, all catalysed reactions proceed via a minimum of charge separation reached in the region of the Au[I]–σ-complex.

Triggered by the results of this study, work is in progress (i) to extend the local mode analysis to non-stationary points, so that we can trace, in the future, bond strength changes along the reaction path; (ii) to further investigate the relationship between reaction path curvature peaks describing bond-forming/breaking events and changes in the bond path topology; (iii) to design Au[I] catalysts for the [3,3]-sigmatropic rearrangement with phosphine substituents increasing the polarity of the CC double bond to be attacked; (iv) to investigate the general performance of our new tool box for the different forms of catalysis.

Acknowledgments

Disclosure statement

No potential conflict of interest was reported by the authors.

Funding

References

[1] S.A. Shahzad, M.A. Sajid, Z.A. Khan, and D. Canseco-Gonzalez, Synth. Commun. **47**(8), 735–755 (2017).

[2] W. Zi and F. Dean Toste, Chem. Soc. Rev. **45**, 4567–4589 (2016).

[3] T. Ishida, H. Koga, M. Okumura, and M. Haruta, Chem. Rec. **16**(5), 2278–2293 (2016).

[4] A.M. Echavarren, A.S.K. Hashmi, and F.D. Toste, Adv. Synth. Catal. **358**(9), 1347–1347 (2016).

[5] A. Villa, N. Dimitratos, C.E. Chan-Thaw, C. Hammond, G.M. Veith, D. Wang, M. Manzoli, L. Prati, and G.J. Hutchings, Chem. Soc. Rev. **45**(18), 4953–4994 (2016).

[6] M. Castineira Reis, C.S. Lopez, E. Kraka, D. Cremer, and O.N. Faza, Inorg. Chem. **55**(17), 8636–8645 (2016).

[7] A.S.K. Hashmi, Top. Organomet. Chem. **44**, 143 (2013).

[8] Y.J. Hong and D.J. Tantillo, Organometallics **30**(21), 5825–5831 (2011).

[9] A.S.K. Hashmi and M. Rudolph, Chem. Soc. Rev. **37**, 1766–1775 (2008).

[10] D.J. Gorin, B.D. Sherry, and F.D. Toste, Chem. Rev. **108**(8), 3351–3378 (2008).

[11] Z. Li, C. Brouwer, and C. He, Chem. Rev. **108**(8), 3239–3265 (2008).

[12] M.S. Scurrell, Gold Bull. **50**(1), 77–84 (2017).

[13] C. Geng, S. Zhang, C. Duan, T. Lu, R. Zhu, C. Liu, and F.D. Toste, RSC Adv. **5**(97), 80048–80056 (2015).

[14] X.C. Cambeiro, N. Ahlsten, and I. Larrosa, J. Am. Chem. Soc. **137**(50), 15636–15639 (2015).

[15] L.T. Ball, G.C. Lloyd-Jones, and C.A. Russell, J. Am. Chem. Soc. **136**(1), 254–264 (2014).

[16] A. Quintavalla and M. Bandini, ChemCatChem. **8**(8), 1437–1453 (2016).

[17] P. Pyykkö, W. Grochala, C. Stampfl, J. Bernholc, R.D. Hoffmann, R. Pöttgen, T. Fickensher, R. Pöttgen, L.H. Tjeng, V. Honkimäki, X.K. Fang, M.L. Kirk, S. Knottenbelt, P. Kögerler, D.G. Musaev, K. Morokuma, M. Takahashi, and C.G. Hill, Chem. Soc. Rev. **37**(9), 1967–1997 (2008).

[18] D.J. Gorin and F.D. Toste, Nature **446**(7134), 395–403 (2007).

[19] E. Kraka, M. Filatov, and D. Cremer, Croat. Chem. Acta **82**(1), 233–243 (2009).

[20] C.R. Kennedy, S. Lin, and E.N. Jacobsen, Angew. Chemie Int. Ed. **55**(41), 12596–12624 (2016).

[21] D.V. Vidhani, J.W. Cran, M.E. Krafft, M. Manoharan, and I.V. Alabugin, J. Org. Chem. **78**(5), 2059–2073 (2013).

[22] A. Corma, A. Leyva-Perez, and M.J. Sabater, Chem. Rev. **111**(3), 1657–1712 (2011).

[23] B.D. Sherry and F.D. Toste, J. Am. Chem. Soc., **126**, 15978–15979 (2004).

[24] A.H. Christian, Z.L. Niemeyer, M.S. Sigman, and F.D. Toste, ACS Catal. **7**, 3973–3978 (2017).

[25] Y. Liu, D. Zhang, and S. Bi, J. Phys. Chem. A **114**(49), 12893–12899 (2010).

[26] A. Levens, F. An, M. Breugst, H. Mayr, and D.W. Lupton, Org. Lett. **18**(15), 3566–3569 (2016).

[27] M.N. Hopkinson, C. Richter, M. Schedler, and F. Glorius, Nature **510**(7506), 485–496 (2014).

[28] A.J. Arduengo, R.L. Harlow, and M. Kline, J. Am. Chem. Soc. **113**(1), 361–363 (1991).

[29] A.J. Arduengo, H.V.R. Dias, R.L. Harlow, and M. Kline, J. Am. Chem. Soc. **114**(14), 5530–5534 (1992).

[30] P.D.W.A. Herrmann, M. Elison, J. Fischer, C. Köcher, and G.R.J. Artus, Angew Chem. Int. Ed. **34**, 2371–2374 (1995).

[31] A. Gómez-Suárez, D.J. Nelson, and S.P. Nolan, Chem. Commun. **53**(18), 2650–2660 (2017).

[32] R. Dorta, A. Ou, L. Wu, A. Salvador, G. Sipos, G. Zhao, B.W. Skelton, and A.N. Sobolev, Dalt. Trans. **46**, 3631–3641 (2017).

[33] S.P. Nolan, Acc. Chem. Res. **44**(2), 91–100 (2011).

[34] N. Marion and S.P. Nolan, Chem. Soc. Rev. **37**(9), 1776–82 (2008).

[35] H. Jacobsen, A. Correa, A. Poater, C. Costabile, and L. Cavallo, Coord. Chem. Rev. **253**(5–6), 687–703 (2009).

[36] K.C. Majumdar, S. Alam, and B. Chattopadhyay, Tetrahedron **64**(4), 597–643 (2008).

[37] L. Claisen, Berichte Dtsch. Chem. Gesellsch. **45**(3), 3157–3166 (1912).

[38] J.W. Ralls, R.E. Lundin, and G.F. Bailey, J. Org. Chem. **28**(12), 3521–3526 (1963).

[39] D.J. Tantillo, Acc. Chem. Res. **49**(4), 741–749 (2016).

[40] D. Tejedor, G. Méndez-Abt, L. Cotos, and F. García-Tellado, Chem. Soc. Rev. **42**(2), 458–471 (2013).

[41] D. Commons, Ph. D. thesis, Department of Chemistry and Biochemistry, Florida State University, 2011, pp. 1–190.

[42] C. Gourlaouen, N. Marion, and S.P. Nolan, Org. Lett. **11**(4), 12–15 (2009).

[43] R.S. Paton and F. Maseras, Org. Lett. **11**(11), 2237–2240 (2009).

[44] S. Porcel, V. López-Carrillo, C. García-Yebra, and A.M. Echavarren, Angew Chem. Int. Ed. **47**(10), 1883–1886 (2008).

[45] M.R. Siebert and D.J. Tantillo, J. Am. Chem. Soc. **129**(28), 8686–8687 (2007).

[46] C.Y. Wu, T. Horibe, C.B. Jacobsen, and F.D. Toste, Nature **517**(7535), 449–54 (2015).

[47] C.N. Kona, M.N. Patil, and C.V. Ramana, Org. Chem. Front. **3**(4), 453–456 (2016).

[48] M.E. Krafft, K.M. Hallal, D.V. Vidhani, and J.W. Cran, Org. Biomol. Chem. **9**, 7535 -7538 (2011).

[49] W. Zou, T. Sexton, E. Kraka, M. Freindorf, and D. Cremer, J. Chem. Theory Comput. **12**, 650–663 (2016).

[50] E. Kraka, Wiley Interdiscip. Rev. Comput. Mol. Sci. **1**(4), 531–556 (2011).

[51] E. Kraka and D. Cremer, Acc. Chem. Res. **43**(5), 591–601 (2010).

[52] D. Cremer and E. Kraka, Curr. Org. Chem. **14**(15), 1524–1560 (2010).

[53] T. Sexton, E. Kraka, and D. Cremer, J. Phys. Chem. A **120**(7), 1097–1111 (2016).

[54] M. Freindorf, T. Sexton, E. Kraka, and D. Cremer, Theor. Chem. Acc. **133**(1), 1423.1–1423.18 (2014).

[55] S. Barua, W. Allen, E. Kraka, P. Jerabek, R. Sure, and G. Frenking, Chem. A Eur. J. **19**(47), 15941–15954 (2013).

[56] H. Joo, E. Kraka, W. Quapp, and D. Cremer, Mol. Phys. **105**(19–22), 2697–2717 (2007).

[57] W.H. Miller, N.C. Handy, and J.E. Adams, J. Chem. Phys. **72**, 99 -112 (1980).

[58] D. Cremer and J.A. Pople, J. Am. Chem. Soc. **97**, 1354–1358 (1975).

[59] D. Cremer, Israel J. Chem. **23**, 72–84 (1983).

[60] D. Cremer and K.J. Szabo, in *Conformational Behavior of Six-Membered Rings*, edited by E. Juaristi (VCH Publishers, New York, 1995), pp. 59–136.

[61] D. Cremer, D. Izotov, W. Zou, and E. Kraka, RING Dallas, 2011.

[62] P.C. Wilson, E.B. Wilson, Decius, and J.C. Cross, *Molecular Vibrations. The Theory of Infrared and Raman Vibrational Spectra* (McGraw-Hill, New York, 1955).

[63] Z. Konkoli and D. Cremer, Int. J. Quantum Chem. **67**(1), 1–9 (1998).

[64] W. Zou, R. Kalescky, E. Kraka, and D. Cremer, J. Chem. Phys. **137**(8), 084114.1–084114.11 (2012).

[65] W. Zou and D. Cremer, Theor. Chem. Acc. **133**(3), 1451–1466 (2014).

[66] R. Kalescky, W. Zou, E. Kraka, and D. Cremer, Chem. Phys. Lett. **554**, 243–247 (2012).

[67] R. Kalescky, E. Kraka, and D. Cremer, Mol. Phys. **111**(9–11), 1497–1510 (2013).

[68] E. Kraka, J. Larsson, and D. Cremer, *Generalization of the Badger Rule Based on the Use of Adiabatic Vibrational Modes* (Wiley-VCH Verlag GmbH Co. KGaA, Weinheim, Germany, 2010).

[69] W. Zou and D. Cremer, Chem. A Eur. J. **22**(12), 4087–4099 (2016).

[70] V. Oliveira, E. Kraka, and D. Cremer, Inorg. Chem. **56**(1), 488–502 (2017).

[71] R. Kalescky, E. Kraka, and D. Cremer, J. Phys. Chem. A **118**(1), 223–237 (2014).

[72] M. Freindorf, E. Kraka, and D. Cremer, Int. J. Quantum Chem. **112**(19), 3174–3187 (2012).

[73] E. Kraka and D. Cremer, ChemPhysChem **10**(4), 686–698 (2009).

[74] C.S. Lopez, O.N. Faza, M. Freindorf, E. Kraka, and D. Cremer, J. Org. Chem. **81**(2), 404–414 (2016).

[75] T. Sexton, E. Kraka, and D. Cremer, J. Phys. Chem. A **120**, 1097–1111 (2016).

[76] K. Fukui, Acc. Chem. Res. **14**(12), 363–368 (1981).

[77] W. Quapp, E. Kraka, and D. Cremer, J. Phys. Chem. A **111**(44), 11287–11293 (2007).

[78] A.D. Becke, J. Chem. Phys. **98**, 5648–5652 (1993).

[79] P. Schwerdtfeger, M. Dolg, W. Schwarz, G. Bowmaker, and P. Boyd, J. Chem. Phys. **91**, 1762–1774 (1989).

[80] D. Andrae, U. Haeussermann, M. Dolg, H. Stoll, and H. Preuss, Theor. Chim. Acta **77**, 123–141 (1990).

[81] R. Ditchfield, W. Hehre, and J. Pople, J. Chem. Phys. **54**, 724–728 (1971).

[82] H.P. Hratchian and E. Kraka, J. Chem. Theory Comput. **9**(3), 1481–1488 (2013).

[83] F. Neese, Wiley Interdiscip. Rev. Comput. Mol. Sci. **2**(1), 73–78 (2012).

[84] C. Riplinger and F. Neese, J. Chem. Phys. **138**, 034106.1-034106.18 (2013).

[85] T.J. Dunning, J. Chem. Phys. **90**, 1007–1023 (1989).

[86] D. Woon and T.J. Dunning, J. Chem. Phys. **98**, 1358–1371 (1993).

[87] D. Woon and T.J. Dunning, J. Chem. Phys. **100**, 2975–2988 (1994).

[88] J. Tomasi, B. Mennucci, and R. Cammi, Chem. Rev. **105**, 2999–3094 (2005).

[89] S. Sinnecker, A. Rajendran, A. Klamt, M. Diedenhofen, and F. Neese, J. Phys. Chem. A **110**, 2235–2245 (2006).

[90] E. Kraka, W. Zou, M. Filatov, J. Grafenstein, D. Izotov, J. Gauss, Y. He, A. Wu, V. Polo, L. Olsson, Z. Konkoli, Z. He, F. Reichel, D. Cremer, *COLOGNE16* (2016).

[91] M. Frisch, G. W. Trucks, H. B. Schlegel, G. E. Scuseria, M. A. Robb, J. R. Cheeseman, G. Scalmani, V. Barone, B. Mennucci, G. A. Petersson, H. Nakatsuji, M. Caricato, X. Li, H. P. Hratchian, A. F. Izmaylov, J. Bloino, G. Zheng, J. L. Sonnenberg, M. Hada, M. Ehara, K. Toyota, R. Fukuda, J. Hasegawa, M. Ishida, T. Nakajima, Y. Honda, O. Kitao, H. Nakai, T. Vreven, J. A. Montgomery, Jr., J. E. Peralta, F. Ogliaro, M. Bearpark, J. J. Heyd, E. Brothers, K. N. Kudin, V. N. Staroverov, R. Kobayashi, J. Normand, K. Raghavachari, A. Rendell, J. C. Burant, S. S. Iyengar, J. Tomasi, M. Cossi, N. Rega, J. M. Millam, M. Klene, J. E. Knox, J. B. Cross, V. Bakken, C. Adamo, J. Jaramillo, R. Gomperts, R. E. Stratmann, O. Yazyev, A. J. Austin, R. Cammi, C. Pomelli, J. W. Ochterski, R. L. Martin, K. Morokuma, V. G. Zakrzewski, G. A. Voth, P. Salvador, J. J. Dannenberg, S. Dapprich, A. D. Daniels, Ö. Farkas, J. B. Foresman, J. V. Ortiz, J. Cioslowski, and D. J. Fox, *Gaussian 09* (Gaussian, Inc., Wallingford CT, 2016).

[92] A. Reed, L. Curtiss, and F. Weinhold, Chem. Rev. **88**, 899–926 (1988).

[93] T.A. Keith, AIMALL TK Gristmill Software, Overland Park, KS, 2017.

[94] S. Boys and F. Bernardi, Mol. Phys. **19**, 553–566 (1970).

[95] A.J. Cohen, P. Mori-Sanchez, W. Yang, P. Mori-Sanchez, W. Yang, P. Mori-Sánchez, and W. Yang, Chem. Rev. **112**(1), 289–320 (2012).

[96] D.H. Ess and K.N. Houk, J. Phys. Chem. A **109**(42), 9542–9553 (2005).

[97] A. Fürstner and P.W. Davies, Angew Chem. Int. Ed. **46**(19), 3410–3449 (2007).

[98] D. Pflästerer and A.S.K. Hashmi, Chem. Soc. Rev. **45**(5), 1331–1367 (2016).

[99] M. Jia and M. Bandini, ACS Catal. **5**(3), 1638–1652 (2015).

[100] R. Bader, *Atoms in Molecules: A Quantum Theory* (Oxford University Press, Oxford, UK, 1994).

[101] D. Cremer and E. Kraka, Croat. Chem. Acta **57**, 1259–1281 (1984).

[102] E. Kraka and D. Cremer, in *Theoretical Models Chemical Bonding*, edited by Z.B. Maksic (Springer Verlag, Heidelberg, 1984), Vol. **2**, pp. 453–478.

[103] S. Zelentsov, V. Hessel, E. Shahbazali, and T. Noël, ChemBioEngRev. **1**(5), 230–240 (2014).

[104] A.M.M. Castro, Chem. Rev. **104**(6), 2939–3002 (2004).

[105] S. Gül, F. Schoenebeck, V. Aviyente, and K.N. Houk, J. Org. Chem. **75**(6), 2115–2118 (2010).